Draft version March 1, 2017
Preprint typeset using LaTeX style AASTeX6 v. 1.0

arXiv:1702.08521v1 [physics.comp-ph] 24 Feb 2017

MULTI-DIMENSIONAL VLASOV-POISSON SIMULATIONS WITH HIGH-ORDER MONOTONICITY AND POSITIVITY PRESERVING SCHEMES

Satoshi Tanaka[1], Kohji Yoshikawa
Center for Computational Sciences, University of Tsukuba, 1-1-1 Tennodai, Tsukuba, Ibaraki 305-8577, Japan

Takashi Minoshima
Department of Mathematical Science and Advanced Technology, Japan Agency for Marine-Earth Science and Technology, 3173-25, Syowa-machi, Kanazawa-ku, Yokohama, Kanagawa 236-0001, Japan

Naoki Yoshida
Department of Physics, The University of Tokyo, Bunkyo, Tokyo 113-0033, Japan
and
Kavli Institute for the Physics and Mathematics of the Universe, The University of Tokyo, Kashiwa, Chiba 277-8583, Japan

[1]stanaka@ccs.tsukuba.ac.jp

ABSTRACT

We develop new numerical schemes for Vlasov–Poisson equations with high-order accuracy. Our methods are based on a spatially monotonicity-preserving (MP) scheme, and are modified suitably so that positivity of the distribution function is also preserved. We adopt an efficient semi-Lagrangian time integration scheme which is more accurate and computationally less expensive than the three-stage TVD Runge-Kutta integration. We apply our spatially fifth- and seventh-order schemes to a suite of simulations of collisionless self-gravitating systems and electrostatic plasma simulations, including linear and nonlinear Landau damping in one-dimension and Vlasov–Poisson simulations in a six-dimensional phase space. The high-order schemes achieve a significantly improved accuracy in comparison with the third-order positive-flux-conserved scheme adopted in our previous study. With the semi-Lagrangian time integration, the computational cost of our high-order schemes does not significantly increase, but remains roughly the same as that of the third-order scheme.

1. INTRODUCTION

Numerical simulations of collisionless self-gravitating systems are one of the indispensable tools in the study of galaxies, galaxy clusters and the large-scale structure of the universe. Gravitational N-body simulations have been widely adopted, and significant scientific achievements have been made for the past four decades. Particles in N-body simulations represent the structure of the distribution function in the phase space in a statistical manner. Similarly, particle-in-cell (PIC) simulations (Birdsall & Langdon 1991) are widely used for studying the dynamics of an astrophysical plasma such as particle acceleration in collisionless shock waves (Matsumoto et al. 2015) and magnetic reconnection (Fujimoto 2014).

Particle-based N-body simulations have several shortcomings, most notably the intrinsic shot noise in the physical quantities such as mass density and velocity field. The discreteness of mass distribution sampled by a finite number of point mass elements (particles) affects the gravitational dynamics considerably in regions with a small number of particles, in other words, where the phase space density is low. For example, gravitational N-body simulations cannot treat collisionless damping of density fluctuations and the two-stream instability in a fluid/plasma with a large velocity dispersion because of poor sampling of particles in the velocity space. Interestingly, physically equivalent situations are observed in PIC simulations (Kates-Harbeck et al. 2016). In PIC simulations, the spacing of grids in the physical space, on which electric and magnetic fields are calculated by solving the Maxwell equations, is constrained not to be larger than the Debye length. Hence the simulation volume is also restricted for a given number of grids.

To overcome these shortcomings, a number of methods alternative to the N-body approach have been proposed. Hernquist & Ostriker (1992) and Hozumi (1997) use the self-consistent field (SCF) method, in which particles move on trajectories on a smooth gravitational potential computed by a basis-function expansion of the density field and gravitational potential. Unlike in conventional N-body simulations, particle motions do not suffer from numerical effects owing to discrete gravitational potential. However, a drawback or complication of the SCF method is that the basis functions need to be suitably chosen for a given configuration of the self-gravitating systems.

Abel et al. (2012), Shandarin et al. (2012) and Hahn et al. (2013) develop a novel method to simulate cosmic structure formation by following the motion of dark matter "sheets" in the phase space volume, while retaining the smooth, continuous structure. The method suppress significantly the artificial discreteness effects in N-body simulations such as a spurious filament fragmentation. The method, however, can only be applied to "cold" matter with sufficiently small velocity dispersions compared with its bulk velocity. Vorobyov & Theis (2006) and Mitchell et al. (2013) solve moment equations of the collisionless Boltzmann equation in a finite volume manner by adopting a certain closure relation. The closure relation needs to be chosen in a problem dependent manner, and often the validity of the adopted relation remains unclear or its applicability is limited.

A straightforward method to simulate a collisionless plasma or a self-gravitating system is directly solving the collisionless Boltzmann equation, or the Vlasov equation. Such an approach was originally explored by Janin (1971) and Fujiwara (1981) for one-dimensional self-gravitating systems, and by Nishida et al. (1981) for two-dimensional stellar disks. It is found to be better in following kinetic phenomena such as collisionless damping and two-stream instability than conventional N-body simulations.

The VlasovPoisson and VlasovMaxwell equations are solved to simulate the dynamics of electrostatic and magnetized plasma, respectively. An important advantage of this approach is that there is no constraint on the mesh spacing, unlike in PIC simulations. In principle, direct Vlasov simulations enable us to simulate the kinematics of an astrophysical plasma with a wide dynamic range, which cannot be easily achieved with PIC simulations.

Despite of its versatile nature, the Vlasov simulations have been applied only to problems in one or two spatial dimensions. Solving the Vlasov equation with three spatial dimensions, i.e., in a six dimensional phase-space, requires an extremely large amount of memory. Yoshikawa et al. (2013) successfully perform Vlasov–Poisson simulations of self-gravitating systems in six-dimensional phase space with achieving high accuracies in mass and energy conservation. Unfortunately, the number of grids is still limited by the amount of available memory rather than the computational cost. With currently available computers, it is not realistic to achieve a significant increase in spatial (and velocity) resolution by simply increasing the number of mesh grids. Clearly, developing high-order schemes is necessary to effectively improve the spatial resolution for a given number of mesh grids. In the present paper, we develop and test new numerical schemes for solving Vlasov equation based on the fifth and seventh order monotonicity preserving (MP) schemes (Suresh & Huynh 1997). We improve the schemes suitably so that the positivity of the distribution function is ensured. We run a suite of test simulations and compare the results with those obtained by the spatially third order positive-flux-conservative (PFC) scheme (Filbet et al. 2001) adopted in our previous work (Yoshikawa et al. 2013) (hereafter YYU13).

The rest of the paper is organized as follows. In section 2, we describe our new numerical schemes to solve the Vlasov equation in higher order accuracy in detail. Section 3 is devoted to present the several test calculations to show the technical advantage of our approach over the previous methods. We address the computational costs of our schemes in section 4. Finally, in section 5, we summarize our results and present our future prospects.

2. VLASOV–POISSON SIMULATION

We follow the time evolution of the distribution function $f(\boldsymbol{x}, \boldsymbol{v}, t)$ according to the following Vlasov (collisionless Boltzmann) equation

$$\frac{\partial f}{\partial t} + \frac{d\boldsymbol{x}}{dt} \cdot \frac{\partial f}{\partial \boldsymbol{x}} + \frac{d\boldsymbol{v}}{dt} \cdot \frac{\partial f}{\partial \boldsymbol{v}} = 0, \tag{1}$$

where $\boldsymbol{x} = (x_1, x_2, x_3) = (x, y, z)$ and $\boldsymbol{v} = (v_1, v_2, v_3) = (v_x, v_y, v_z)$ are the Cartesian spatial and velocity coordinates, respectively. For self-gravitating systems, it gives the Vlasov–Poisson equation as

$$\frac{\partial f}{\partial t} + \boldsymbol{v} \cdot \frac{\partial f}{\partial \boldsymbol{x}} - \frac{\partial \phi}{\partial \boldsymbol{x}} \cdot \frac{\partial f}{\partial \boldsymbol{v}} = 0, \tag{2}$$

where ϕ is the gravitational potential satisfying the Poisson equation

$$\nabla^2 \phi = 4\pi G \rho = 4\pi G \int f \, \mathrm{d}^3 \boldsymbol{v}, \tag{3}$$

where G is the gravitational constant and ρ is the mass density. Throughout the present paper, the distribution function is normalized such that its integration over velocity space yields the mass density. We discretize the distribution function $f(\boldsymbol{x}, \boldsymbol{v}, t)$ in the same manner as in YYU13; we employ a uniform Cartesian mesh in both the physical configuration space and in the velocity (momentum) space.

2.1. *Advection Solver*

The Vlasov equation (2) can be broken down into six one-dimensional advection equations along each dimension of the phase space; three for advection in the physical space

$$\frac{\partial f}{\partial t} + v_i \frac{\partial f}{\partial x_i} = 0 \qquad (i = 1, 2, 3), \tag{4}$$

and another three in the velocity space

$$\frac{\partial f}{\partial t} - \frac{\partial \phi}{\partial x_i} \frac{\partial f}{\partial v_i} = 0 \qquad (i = 1, 2, 3). \tag{5}$$

We solve these six equations sequentially. The gravitational potential ϕ in equations (5) is updated after advection equations (4) in the physical space are solved and the mass density distribution in the physical space is updated. Clearly, an accurate numerical scheme for one-dimensional advection scheme is a crucial ingredient of our Vlasov solver.

Let us consider a numerical scheme of the following advection equation

$$\frac{\partial f(x,t)}{\partial t} + c \frac{\partial f(x,t)}{\partial x} = 0, \tag{6}$$

on a one-dimensional uniform mesh grid. In a finite-volume manner, we define an averaged value of $f(x,t)$ over the i-th grid centered at $x = x_i$ with the interval of Δx at a time $t = t^n$ as

$$f_i^n = \frac{1}{\Delta x} \int_{x_{i-1/2}}^{x_{i+1/2}} f(x, t^n)\, \mathrm{d}x, \tag{7}$$

where $x_{i\pm1/2} = x_i \pm \Delta x/2$ are the coordinates of the boundaries of the i-th mesh grid. Without loss of generality, we can restrict ourselves to the case with a positive advection velocity $c > 0$.

Physical and mathematical considerations impose the following requirements on numerical solutions of the advection equation: (i) Monotonicity—since the solution of the advection equation (6) preserves monotonicity, so should its numerical solution. (ii) Positivity—the distribution function must be positive by definition, and thus the numerical solution should be non-negative. Note that monotonicity is not sufficient to ensure positivity of the numerical solution.

2.1.1. *MP schemes with the positivity preserving limiter*

We first present the spatially fifth-order scheme for the advection equation (6) based on the MP5 scheme of Suresh & Huynh (1997), in which the value of $f(x,t)$ at the interface between the $(i-1)$-th and i-th mesh grids is reconstructed with five stencils f_{i-3}^n, f_{i-2}^n, f_{i-1}^n, f_i^n and f_{i+1}^n as

$$f_{i-1/2}^{\mathrm{int},5} = (2f_{i-3} - 13f_{i-2} + 47f_{i-1} + 27f_i - 3f_{i+1})/60. \tag{8}$$

In order to ensure monotonicity of the numerical solution, we impose the constraint

$$\bar{f}_{i-1/2} = \mathrm{MP}(f_{i-1/2}^{\mathrm{int},5}, f_{i-3}, f_{i-2}, f_{i-1}.f_i, f_{i+1}) \tag{9}$$

The detailed prescription of the constraints are given in Appendix A. The MP5 scheme adopts the three-stage TVD Runge-Kutta (TVD-RK) time integration as

$$\begin{aligned} f_i^{(1)} &= f_i^n - \nu L_i(f^n) \\ f_i^{(2)} &= \frac{3}{4} f_i^n + \frac{1}{4}\left(f_i^{(1)} - \nu L_i(f^{(1)})\right) \\ f_i^{n+1} &= \frac{1}{3} f_i^n + \frac{2}{3}\left(f_i^{(2)} - \nu L_i(f^{(2)})\right), \end{aligned} \tag{10}$$

where $\nu = c\Delta t/\Delta x$ is the CFL number and the operator $L_i(f)$ is defined as

$$L_i(f) = \bar{f}_{i+1/2} - \bar{f}_{i-1/2}. \tag{11}$$

Hereafter, this scheme is refered to as RK–MP5.

As already noted above, the MP scheme does not ensure positivity of the numerical solution. We thus introduce a positivity preserving limiter based on the method proposed by Hu et al. (2013). By denoting $U_i^+ = f_i^n - 2\nu\bar{f}_{i+1/2}^n$ and $U_i^- = f_i^n + 2\nu\bar{f}_{i-1/2}^n$, the single-stage Eulerian time integration can be written as

$$f_i^{(1)} = f_i^n - \nu(\bar{f}_{i+1/2}^n - \bar{f}_{i-1/2}^n) \tag{12}$$

$$= \frac{1}{2}\left(f_i^n - 2\nu\bar{f}_{i+1/2}^n\right) + \frac{1}{2}\left(f_i^n + 2\nu\bar{f}_{i-1/2}^n\right) \tag{13}$$

$$= \frac{1}{2}U_i^+ + \frac{1}{2}U_i^-. \tag{14}$$

Here, we consider a linear combination of the interface value obtained with the MP scheme and that with the spatially first-order upwind scheme as

$$\hat{f}_{i+1/2}^n = \theta_{i+1/2}\bar{f}_{i+1/2}^n + (1-\theta_{i+1/2})f_{i+1/2}^{\mathrm{UP},n}, \tag{15}$$

where $f_{i+1/2}^{\mathrm{UP},n}$ is expressed as

$$f_{i+1/2}^{\mathrm{UP},n} = \frac{1}{2c}\left[f_i^n(c+|c|) + f_{i+1}^n(c-|c|)\right] = f_i^n, \tag{16}$$

and $\theta_{i+1/2}$ is a parameter with condition of $0 \le \theta_{i+1/2} \le 1$. Note that the spatially first-order upwind scheme preserves positivity of the numerical solution if the CFL condition $\nu \le 1$ is satisfied. Then, the time integration of the combined interface values (15) can be written as

$$f_i^{(1)} = f_i^n - \nu(\hat{f}_{i+1/2}^n - \hat{f}_{i-1/2}^n) \tag{17}$$

$$= \frac{1}{2}\left(f_i^n - 2\nu\hat{f}_{i+1/2}^n\right) + \frac{1}{2}\left(f_i^n + 2\nu\hat{f}_{i-1/2}^n\right) \tag{18}$$

$$= \frac{1}{2}\left\{\theta_{i+1/2}U_i^+ + (1-\theta_{i+1/2})U_i^{\mathrm{UP},+}\right\} + \frac{1}{2}\left\{\theta_{i-1/2}U_i^- + (1-\theta_{i-1/2})U_i^{\mathrm{UP},-}\right\}, \tag{19}$$

where $U_i^{\mathrm{UP},+} = f_i^n - 2\nu f_{i+1/2}^{\mathrm{UP},n}$ and $U_i^{\mathrm{UP},-} = f_i^n + 2\nu f_{i-1/2}^{\mathrm{UP},n}$. Therefore, if both of the two terms in the rhs of equation (19) are positive, $f_i^{(1)}$ is also positive. A simple calculation shows that it can be realized by setting the parameter $\theta_{i+1/2}$ as

$$\theta_{i+1/2} = \min(\theta_{i+1/2}^+, \theta_{i+1/2}^-), \tag{20}$$

where

$$\theta_{i+1/2}^+ = \begin{cases} \dfrac{U_i^{\mathrm{UP},+}}{U_i^{\mathrm{UP},+} - U_i^+} & \text{if } U_i^+ < 0 \\ 1 & \text{otherwise} \end{cases} \tag{21}$$

and

$$\theta_{i+1/2}^- = \begin{cases} \dfrac{U_{i+1}^{\mathrm{UP},-}}{U_{i+1}^{\mathrm{UP},-} - U_{i+1}^-} & \text{if } U_{i+1}^- < 0 \\ 1 & \text{otherwise.} \end{cases} \tag{22}$$

In addition, the condition of $\theta_{i+1/2} \ge 0$ can be met by setting $U_i^{\mathrm{UP},+} \ge 0$ and $U_{i+1}^{\mathrm{UP},-} \ge 0$ as a sufficient condition, which leads to a constraint on the CFL parameter as $\nu \le 1/2$. Let us denote the above procedures to evaluate the positive interface value (15) as

$$\hat{f}_{i+1/2}^n = \mathrm{PP}(\bar{f}_{i+1/2}^n, f_i^n, f_{i+1}^n). \tag{23}$$

It can be shown that positivity of the numerical solution is preserved even with the three-stage TVD-RK time integration by setting the CFL parameter to $\nu < 1/2$. In the following, we call this scheme RK–MPP5 scheme (MPP for "monotonicity and positivity preserving").

It is tedious but straightforward to construct the spatially seventh-order schemes, RK–MP7 and RK–MPP7, by simply replacing $f_{i-1/2}^{\mathrm{int},5}$ in equation (9) with the seventh-order interpolation

$$f_{i-1/2}^{\mathrm{int},7} = (-3f_{i-4} + 25f_{i-3} - 101f_{i-2} + 319f_{i-1} + 214f_i - 38f_{i+1} + 4f_{i+2})/420. \tag{24}$$

2.1.2. *Semi-Lagrangian Time Integration*

The MP schemes described above adopt the three-stage TVD-RK time integration (10), which needs explicit Euler integration three times per single time step. It can be a source of significant computational cost. To overcome this drawback, we devise an alternative method based on the semi-Lagrangian (SL) time integration.

The averaged value of $f(x,t)$ over the i-th mesh grid f_i^{n+1} at a time of $t^{n+1} = t^n + \Delta t$ is written as

$$f_i^{n+1} = \frac{1}{\Delta x}\int_{x_{i-1/2}}^{x_{i+1/2}} f(x,t^{n+1})\,\mathrm{d}x = \frac{1}{\Delta x}\int_{X(t^n,t^{n+1},x_{i-1/2})}^{X(t^n,t^{n+1},x_{i+1/2})} f(x,t^n)\,\mathrm{d}x, \tag{25}$$

where $X(t_1,t_2,x)$ is the position of the characteristic curve at a time of t_1 originating from the phase space coordinate (x,t_2), and for the advection equation (6), $X(t_1,t_2,x) = x - c(t_2-t_1)$, see Figure 1. Denoting

$$\Phi_{i+1/2}^n = \frac{1}{c\Delta t}\int_{X(t^n,t^{n+1},x_{i+1/2})}^{x_{i+1/2}} f(x,t^n)\,\mathrm{d}x \tag{26}$$

and

$$\Phi_{i-1/2}^n = \frac{1}{c\Delta t}\int_{X(t^n,t^{n+1},x_{i-1/2})}^{x_{i-1/2}} f(x,t^n)\,\mathrm{d}x, \tag{27}$$

we can rewrite the equation (25) in terms of numerical flux as

$$f_i^{n+1} = f_i^n - \nu(\Phi_{i+1/2}^n - \Phi_{i-1/2}^n). \tag{28}$$

By interpolating the discrete values of f_j^n, we can compute the numerical fluxes $\Phi_{i+1/2}$ and $\Phi_{i-1/2}$. Actually, the positive flux conservative (PFC) scheme also adopts essentially the same approach. It adopts the third-order reconstruction to interpolate f_j^n with a slope limiter and suppresses numerical oscillation while preserving positivity of the numerical solutions. For more detailed description of the PFC scheme, see Filbet et al. (2001) and the Appendix of YYU13.

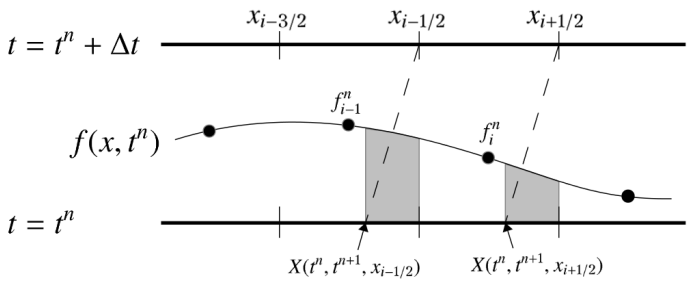

Figure 1. Schematic description of the semi-Lagrangian scheme. Dashed lines starting from $x_{i\pm1/2}$ are the characteristic curves. The areas of the left and right shaded regions correspond to $\Phi_{i-1/2}$ and $\Phi_{i+1/2}$, respectively.

Our new schemes are based on the conservative semi-Lagrangian (CSL) scheme (Qiu & Christlieb 2010; Qiu & Shu 2011), which is originally coupled with a finite difference scheme but is also applicable to the finite volume schemes. In the fifth-order CSL scheme, $\Phi_{i-1/2}^n$ can be expressed with five stencil values as

$$\Phi_{i-1/2}^n = \sum_{j=0}^{4} C_j \zeta^j \tag{29}$$

where

$$C_0 = \frac{f_{i-3}^n}{30} - \frac{13}{60}f_{i-2}^n + \frac{47}{60}f_{i-1}^n + \frac{9}{20}f_i^n - \frac{f_{i+1}^n}{20} \tag{30}$$

$$C_1 = -\frac{f_{i-2}^n}{24} + \frac{5}{8}f_{i-1}^n - \frac{5}{8}f_i^n + \frac{f_{i+1}^n}{24} \tag{31}$$

$$C_2 = -\frac{f_{i-3}^n}{24} + \frac{f_{i-2}^n}{4} - \frac{f_{i-1}^n}{3} + \frac{f_i^n}{12} + \frac{f_{i+1}^n}{24} \tag{32}$$

$$C_3 = \frac{f_{i-2}^n}{24} - \frac{f_{i-1}^n}{8} + \frac{f_i^n}{8} - \frac{f_{i+1}^n}{24} \tag{33}$$

$$C_4 = \frac{f^n_{i-3}}{120} - \frac{f^n_{i-2}}{30} + \frac{f^n_{i-1}}{20} - \frac{f^n_i}{30} + \frac{f^n_{i+1}}{120} \tag{34}$$

and

$$\zeta = \frac{c\Delta t}{\Delta x}. \tag{35}$$

The seventh-order CSL scheme is given by

$$\Phi^n_{i-1/2} = \sum_{j=0}^{6} D_j \zeta^j, \tag{36}$$

where

$$D_0 = -\frac{f^n_{i-4}}{140} + \frac{5}{84} f^n_{i-3} - \frac{101}{420} f^n_{i-2} + \frac{319}{420} f^n_{i-1} + \frac{107}{210} f^n_i - \frac{19}{210} f^n_{i+1} + \frac{f^n_{i+2}}{105} \tag{37}$$

$$D_1 = \frac{f^n_{i-3}}{180} - \frac{5}{72} f^n_{i-2} + \frac{49}{72} f^n_{i-1} - \frac{49}{72} f^n_i + \frac{5}{72} f^n_{i+1} - \frac{f^n_{i+2}}{180} \tag{38}$$

$$D_2 = \frac{7}{720} f^n_{i-4} - \frac{19}{240} f^n_{i-3} + \frac{7}{24} f^n_{i-2} - \frac{23}{72} f^n_{i-1} + \frac{f^n_i}{48} + \frac{7}{80} f^n_{i+1} - \frac{f^n_{i+2}}{90} \tag{39}$$

$$D_3 = -\frac{f^n_{i-3}}{144} + \frac{11}{144} f^n_{i-2} - \frac{7}{36} f^n_{i-1} + \frac{7}{36} f^n_i - \frac{11}{144} f^n_{i+1} + \frac{f^n_{i+2}}{144} \tag{40}$$

$$D_4 = -\frac{f^n_{i-4}}{360} + \frac{f^n_{i-3}}{48} - \frac{13}{240} f^n_{i-2} + \frac{23}{360} f^n_{i-1} - \frac{f^n_i}{30} + \frac{f^n_{i+1}}{240} + \frac{f^n_{i+2}}{720} \tag{41}$$

$$D_5 = \frac{f^n_{i-3}}{720} - \frac{f^n_{i-2}}{144} + \frac{f^n_{i-1}}{72} - \frac{f^n_i}{72} + \frac{f^n_{i+1}}{144} - \frac{f^n_{i+2}}{720} \tag{42}$$

and

$$D_6 = \frac{f^n_{i-4}}{5040} - \frac{f^n_{i-3}}{840} + \frac{f^n_{i-2}}{336} - \frac{f^n_{i-1}}{252} + \frac{f^n_i}{336} - \frac{f^n_{i+1}}{840} + \frac{f^n_{i+2}}{5040}. \tag{43}$$

However, the numerical solution obtained with the CSL scheme does not preserve the monotonicity. Thus, we apply the MP constraint to $\Phi^n_{i-1/2}$ and $\Phi^n_{i+1/2}$ as

$$\bar{\Phi}^n_{i-1/2} = \mathrm{MP}(\Phi^n_{i-1/2}, f^n_{i-3}, f^n_{i-2}, f^n_{i-1}, f^n_i, f^n_{i+1}) \tag{44}$$

and

$$\bar{\Phi}^n_{i+1/2} = \mathrm{MP}(\Phi^n_{i+1/2}, f^n_{i-2}, f^n_{i-1}, f^n_i, f^n_{i+1}, f^n_{i+2}). \tag{45}$$

The numerical solution with the monotonicity preservation at $t = t^{n+1}$ is then computed as

$$f^{n+1}_i = f^n_i - \nu(\bar{\Phi}^n_{i+1/2} - \bar{\Phi}^n_{i-1/2}), \tag{46}$$

which is refered to as SL–MP5 and SL–MP7 schemes (SL for "semi-Lagrangian") for the fifth- and seventh-order accuracies, respectively.

The positivity preserving limiter described in the previous subsection can be applied as

$$\hat{\Phi}^n_{i-1/2} = \mathrm{PP}(\bar{\Phi}^n_{i-1/2}, f^n_{i-1}, f^n_i) \tag{47}$$

and

$$\hat{\Phi}^n_{i+1/2} = \mathrm{PP}(\bar{\Phi}^n_{i+1/2}, f^n_i, f^n_{i+1}). \tag{48}$$

Then, the numerical solution at t^{n+1} is given by

$$f^{n+1}_i = f^n_i - \nu(\hat{\Phi}^n_{i+1/2} - \hat{\Phi}^n_{i-1/2}). \tag{49}$$

We refer to these schemes as the SL–MPP5 and SL–MPP7 scheme hereafter.

2.2. *Poisson Solver*

The Poisson equation (3) is numerically solved with the convolution method (Hockney & Eastwood 1981) using the fast Fourier transform (FFT). Under periodic boundary conditions, the discrete Fourier transform (DFT) of the gravitational potential $\phi(\boldsymbol{k})$ can be written as

$$\hat{\phi}(\boldsymbol{k}) = G(\boldsymbol{k})\hat{\rho}(\boldsymbol{k}) \tag{50}$$

where $\hat{\rho}(\boldsymbol{k})$ is the DFT of the density field, $\boldsymbol{k} = (k_x, k_y, k_z)$ is the discrete wavenumber vector, and $G(\boldsymbol{k})$ is the Fourier-transformed Green function of the discretized Poisson equation. The second-order discretization of the Green function, $G(\boldsymbol{k})$, is given by

$$G(\boldsymbol{k}) = -\frac{\pi G\Delta^2}{\displaystyle\sum_{i=x,y,z} \sin^2\left(\frac{k_i\Delta}{2}\right)} \tag{51}$$

with $\Delta x = \Delta y = \Delta z = \Delta$. Since we adopt advection solvers with spatially fifth- and seventh-order accuracy, it is reasonable to adopt a Poisson solver with the same or similar order of accuracy, which can be simply constructed by high-order discretization of the Poisson equation. As shown in Appendix C, the DFT of the Green functions with spatially fourth- and sixth-order accuracy are given by

$$G(\boldsymbol{k}) = \frac{12\pi G\Delta^2}{\displaystyle\sum_{i=x,y,z} \left[\sin^2(k_i\Delta) - 16\sin^2\left(\frac{k_i\Delta}{2}\right)\right]} \tag{52}$$

and

$$G(\boldsymbol{k}) = -\frac{180\pi G\Delta^2}{\displaystyle\sum_{i=x,y,z} \left[2\sin^2\left(\frac{3k_i\Delta}{2}\right) - 27\sin^2(k_i\Delta) + 270\sin^2\left(\frac{k_i\Delta}{2}\right)\right]}, \tag{53}$$

respectively. The gravitational potential $\phi(\boldsymbol{x})$ is computed with the inverse DFT of $\hat{\phi}(\boldsymbol{k})$.

For isolated boundary conditions, the doubling-up method (Hockney & Eastwood 1981) is adopted, where the number of mesh grids is doubled for each spatial dimension and the mass density in the extended grid points are zeroed out. The Green function is set up in the real space as

$$G(x, y, z) = \frac{G}{(x^2 + y^2 + z^2)^{1/2}} \tag{54}$$

and is Fourier transformed to obtain $\hat{G}(\boldsymbol{k})$. Then, the gravitational potential can be calculated in the same manner as in the the periodic boundary condition.

After obtaining the gravitational potential, we compute gravitational forces at each of the spatial grids with the finite difference approximation (FDA). Again we adopt FDA schemes with the same order of accuracy with that of the gravitational potential calculation. The two-, four- and six-point FDA are described in Appendix C. In what follows, we adopt the sixth-order calculation of the gravitational forces and potentials irrespective of adopted advection schemes because we are primarily interested in the accuracy of our advection equation solver.

2.3. *Parallelization and Domain Decomposition*

We parallelize our Vlasov–Poisson solvers by decomposing the six-dimensional phase space into distributed memory spaces. We decompose the computational domain in the phase space in the same manner as YYU13. The physical space is divided into rectangular subdomains along x-, y- and z-directions, while the velocity space is not decomposed; each spatial point has an entire set of velocity mesh grids. This decomposition is convenient when computing the velocity moments of the distribution function such as the mass density, mean velocities and velocity dispersions.

In solving the advection equations in the physical space (4) across the decomposed subdomains, the values of the distribution function adjacent to the boundaries of the subdomains are transferred using the Message Passing Interface (MPI). The number of the adjacent mesh grids to be transferred is two for the spatially third-order PFC scheme, and three and four for spatially fifth- and seventh-order MP schemes, respectively.

2.4. *Time Integration*

We advance the distribution function from $t = t^n$ to t^{n+1} using the directional splitting method in the order of

$$\begin{aligned} f(\boldsymbol{x}, \boldsymbol{v}, t^{n+1}) = & T_{v_z}(\Delta t/2) T_{v_y}(\Delta t/2) T_{v_x}(\Delta t/2) \\ & \times T_x(\Delta t) T_y(\Delta t) T_z(\Delta t) \\ & \times T_{v_z}(\Delta t/2) T_{v_y}(\Delta t/2) T_{v_x}(\Delta t/2) f(\boldsymbol{x}, \boldsymbol{v}, t^n), \end{aligned} \tag{55}$$

where $T_\ell(\Delta t)$ denotes an operator for advection along the ℓ-direction with time step Δt. It should be noted that the Poisson equation is solved after the advection operations in the physical space ($T_x T_y T_z$) to update the gravitational potential and forces for the updated density field.

As for time step width, we have several constraints on the CFL parameter. The MP schemes are subject to the constraint with $\nu \leq 1/5$ if the parameter α in the MP scheme is set to $\alpha = 4$ (see Appendix A) and the PP limiter requires $\nu \leq 1/2$. As shown in Appendix B, all of our new schemes work well for $3 < \alpha$ and $\nu < 0.4$. In practice, the condition $\nu = 1/(1+\alpha)$ is desirable, and thus we set $\alpha = 4$ and $\nu = 0.2$ throughout the present paper. [1]

We set the time step for integrating the Vlasov equation as

$$\Delta t = \min(\Delta t_{\rm p}, \Delta t_{\rm v}), \tag{56}$$

where $\Delta t_{\rm p}$ and $\Delta t_{\rm v}$ are the time step for advection equations in physical and velocity space, respectively. $\Delta t_{\rm p}$ is given by

$$\Delta t_{\rm p} = \nu \min\left(\frac{\Delta x}{V_x^{\rm max}}, \frac{\Delta y}{V_y^{\rm max}}, \frac{\Delta z}{V_z^{\rm max}} \right), \tag{57}$$

where $\Delta \ell$ denotes the spacing of mesh grids along the ℓ-direction and $V_\ell^{\rm max}$ is the maximum extent of the velocity mesh along v_ℓ-direction. Similarly, we compute $\Delta t_{\rm v}$ as

$$\Delta t_{\rm v} = \nu \min_i \left(\frac{\Delta v_x}{|a_{x,i}|}, \frac{\Delta v_y}{|a_{y,i}|}, \frac{\Delta v_z}{|a_{z,i}|} \right), \tag{58}$$

where $a_{\ell,i}$ is the gravitational acceleration along ℓ-direction at the i-th mesh grids in the physical space and the minimization is taken over all the spatial mesh grids.

3. TEST CALCULATIONS

In this section, we present the results of several test simulations with our new schemes. The test suite includes simulations of one-dimensional advection, and Vlasov–Poisson simulations in two- and six-dimensional phase space.

3.1. *Test-1: One-dimensional Advection*

The first test run we perform is the one-dimensional advection problem. We solve

$$\frac{\partial f(x,t)}{\partial t} + \frac{\partial f(x,t)}{\partial x} = 0 \tag{59}$$

with our new schemes. Since the accuracy of the numerical solutions depends on the shape of $f(x,t)$, we consider three initial conditions and examine critically the numerical solutions.

3.1.1. *Test-1a: Rectangular shaped function*

We configure the rectangular shaped initial condition given by

$$f(x, t=0) = \begin{cases} 1 & 0.25 \leq x \leq 0.75 \\ 0 & \text{otherwise} \end{cases} \tag{60}$$

in the simulation domain over $0 \leq x \leq 1$ and integrate equation (59) using PFC, RK–MPP5, RK–MPP7, SL–MPP5 and SL–MPP7 under the periodic boundary conditions. Figure 2 shows the profiles of $f(x,t)$ at $t = 8$ with the number of meshes $N_{\rm m} = 64$. The numerical solutions with RK–MPP5, SL–MPP5 and SL–MPP7 are less diffusive compared with that of PFC. RK–MPP7 exhibits asymmetric features around $x \simeq 0.2$ and 0.7. Actually these features are

[1] The PFC scheme is free from any explicit constraints on time step thanks to its semi-Lagrangian nature in solving one-dimensional advection equation. Nonetheless, it is better to adopt a certain constraint in domain-decomposed (and hence parallelized) Vlasov simulations in multi-dimensional phase space. With large time steps, the trajectories of characteristic lines originating from the boundaries of decomposed domains reach further from the boundaries, and the number of grids to be passed to the adjacent domains becomes also larger resulting in the increase of the amount of data exchange between parallel processes.

persistent irrespective of $N_{\rm m}$ and ν. It is likely caused by the lack of accuracy in the time integration. We do not run the rest of our test simulations with RK–MP7 and RK–MPP7. Figure 3 show the relative error of the numerical solutions to the analytic solution defined as

$$\epsilon = \frac{\sum_{i=1}^{N_{\rm m}} |f_i^n - f(x_i, t^n)|}{\sum_{i=1}^{N_{\rm m}} |f(x_i, t^n)|}. \tag{61}$$

Since there are discontinuities in the initial condition, the numerical fluxes computed with PFC and MP schemes are effectively of the first order, avoiding numerical oscillations. This is why the relative errors scales with the first-order power law.

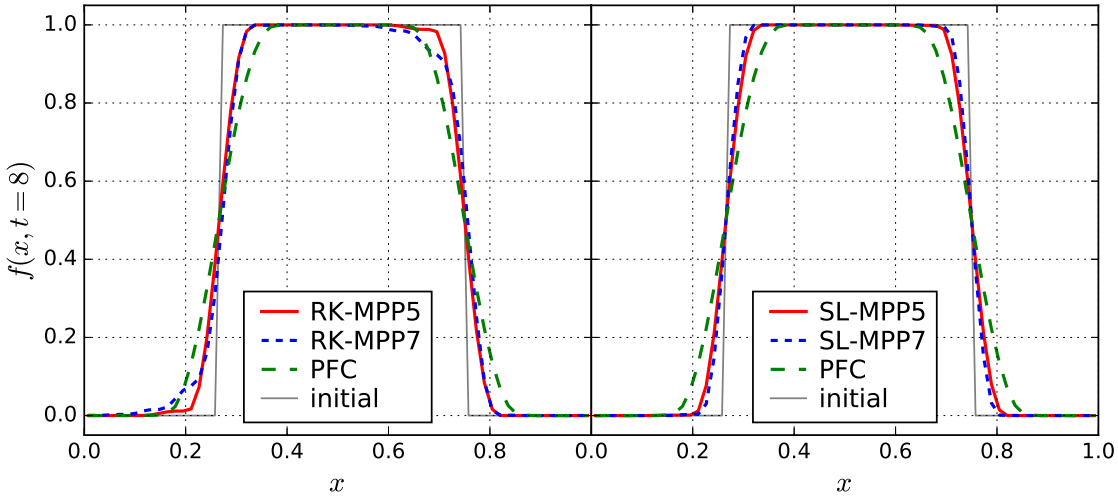

Figure 2. Test-1a (rectangular shaped function): Profiles of the initially rectangular-shaped function at $t = 8$ computed with the PFC, RK–MPP5, RK–MPP7, SL–MPP5, and SL–MPP7 schemes. We set $N_{\rm m} = 64$.

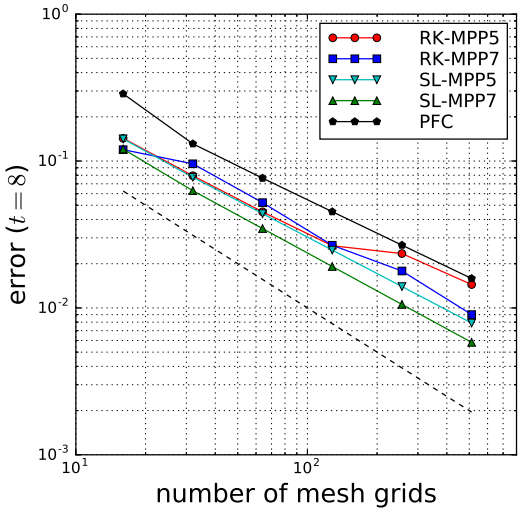

Figure 3. Test-1a (rectangular shaped function): Relative errors of the numerical solutions with PFC, RK–MPP5, RK–MPP7, SL–MPP5 and SL-MPP7 schemes. A thin dashed line indicates the error scaling proportional to $N_{\rm m}^{-1}$.

3.1.2. *Test-1b:Sinusoidal wave*

As a good example of advection of a smooth function, we consider the initial condition given by

$$f(x, t = 0) = 1 + \sin(2\pi x), \tag{62}$$

in the periodic domain of $0 \leq x \leq 1$. Figure 4 shows the relative errors of numerical solutions obtained with RK–MPP5, SL–MPP5 and SL–MPP7 in the left panel and with RK–MP5, SL–MP5 and SL–MP7 without the positivity preserving (PP) limiter in the right panel as a function of $N_{\rm m}$. For comparison, the result obtained with PFC is also presented in both the panels. The numerical solutions obtained with RK–MPP5 have nearly third-order accuracy for $N_{\rm m} \gtrsim 10^2$, whereas those with RK–MP5 have the fifth-order accuracy. This is because the PP limiter operates at the minima of numerical solutions at each stage of the TVD-RK time integration and degrades overall accuracy. Contrastingly, the accuracies of the SL schemes are not affected by the PP limiter, i.e., the results of SL–MPP5 and SL–MPP7 show fifth- and seventh-order scaling.

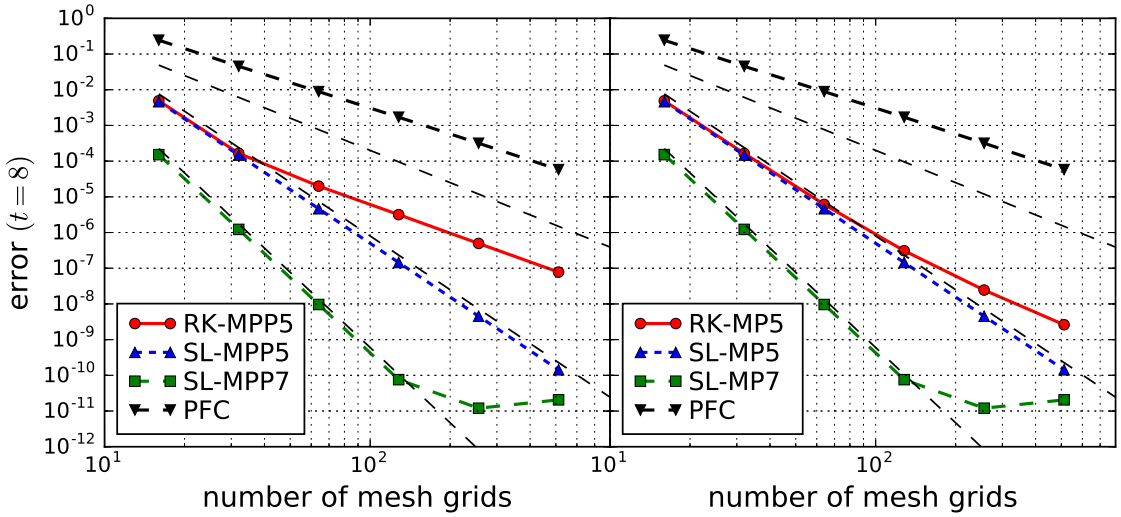

Figure 4. Test-1b (sinusoidal wave): Relative errors of the advection of sinusoidal waves computed with schemes with and without the positivity preserving limiter in the left and right panels, respectively. Thin dashed lines in each panels indicate the scalings of the numerical errors in the third-, fifth- and seventh-order accuracies from top to bottom.

3.1.3. *Test-1c:* $\sin^4(4\pi x)$ *function*

The final example is the initial condition given by

$$f(x, t = 0) = \sin^4(4\pi x). \tag{63}$$

This case serves as a good example to examine how well the PP limiter works. Figure 5 shows the numerical solutions with $N_{\rm m} = 64$ computed at $t = 8$ with the PFC, RK–MP5 and RK–MPP5 (left panel), and those obtained with SL–MP5, SL–MPP5 and SL–MPP7 schemes (right panel). The PFC solution is significantly smeared near the maxima and minima, although it preserves positivity. The numerical solutions obtained with RK–MP5 and SL–MP5 without the PP limiter exhibit noticeable negative values around the minima. On the other hand, the RK–MPP5, SL–MPP5 and SL–MPP7 successfully preserve positivity and reproduce the analytic solution very well. Note that SL–MPP7 is better in reproducing the profiles around the maxima than SL–MPP5 and RK–MPP5, showing the importance of high-order accuracy. As can be seen in Figure 6, the order of accuracy for RK–MPP5, SL–MPP5 and SL–MPP7 is actually close to the fifth, and the result with SL–MPP7 is more accurate.

3.2. *Test-2: One-dimensional Gravitational Instability*

Next, we perform simulations of spatially one-dimensional self-gravitating systems in two-dimensional phase space volume. We consider the periodic simulation domain with $0 \leq x \leq L$ and set the initial condition to be

$$f(x, v, t = 0) = \frac{\bar{\rho}[1 + A\sin(kx)]}{(2\pi\sigma^2)^{1/2}} \exp\left(-\frac{v^2}{2\sigma^2}\right), \tag{64}$$

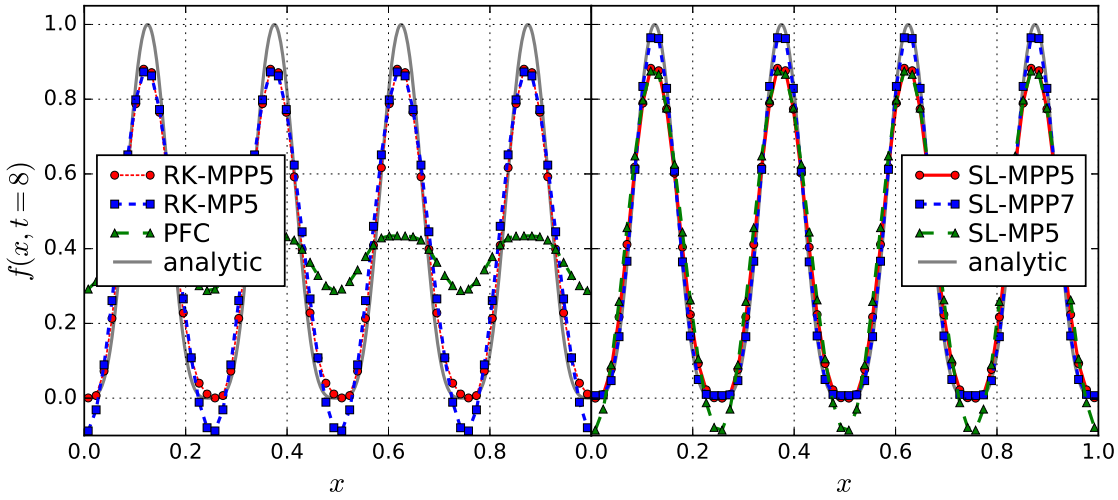

Figure 5. Test-1c ($\sin^4(4\pi x)$ function): Profiles of the numerical solutions with the RK-schemes (left panel) and the SL-schemes (right panel). For comparison, we present the result obtained with the PFC scheme in the left panel. We set $N_{\rm m} = 64$.

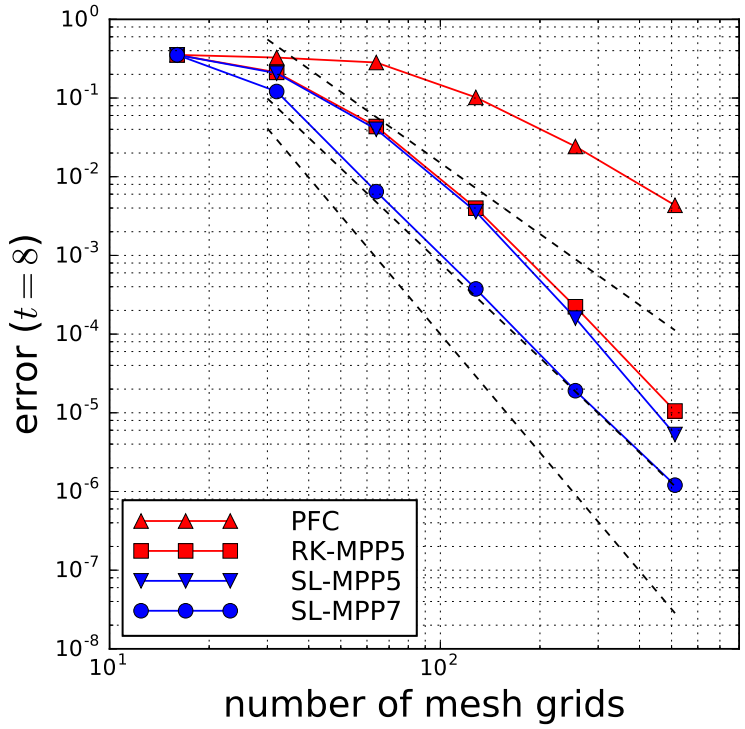

Figure 6. Test-1c ($\sin^4(4\pi x)$ function): Relative errors of the PFC, RK–MPP5, SL–MPP5 and SL–MP7 in Test-1c. Thin dashed lines show the error scaling of third-, fifth- and seventh-order accuracies from top to bottom.

where σ is the velocity dispersion, $\bar{\rho}$ is the mean density of the system and A is the amplitude of density inhomogeneity. This distribution function yields the initial mass density as

$$\rho(x) = \bar{\rho}[1 + A\cos(kx)], \tag{65}$$

and the density inhomogeneity develops through the gravitational instability when the wavenumber k satisfies the condition $k/k_{\rm J} < 1$, where $k_{\rm J}$ is the Jeans wavenumber defined by

$$k_{\rm J} = \left(\frac{4\pi G\bar{\rho}}{\sigma^2}\right)^{1/2}. \tag{66}$$

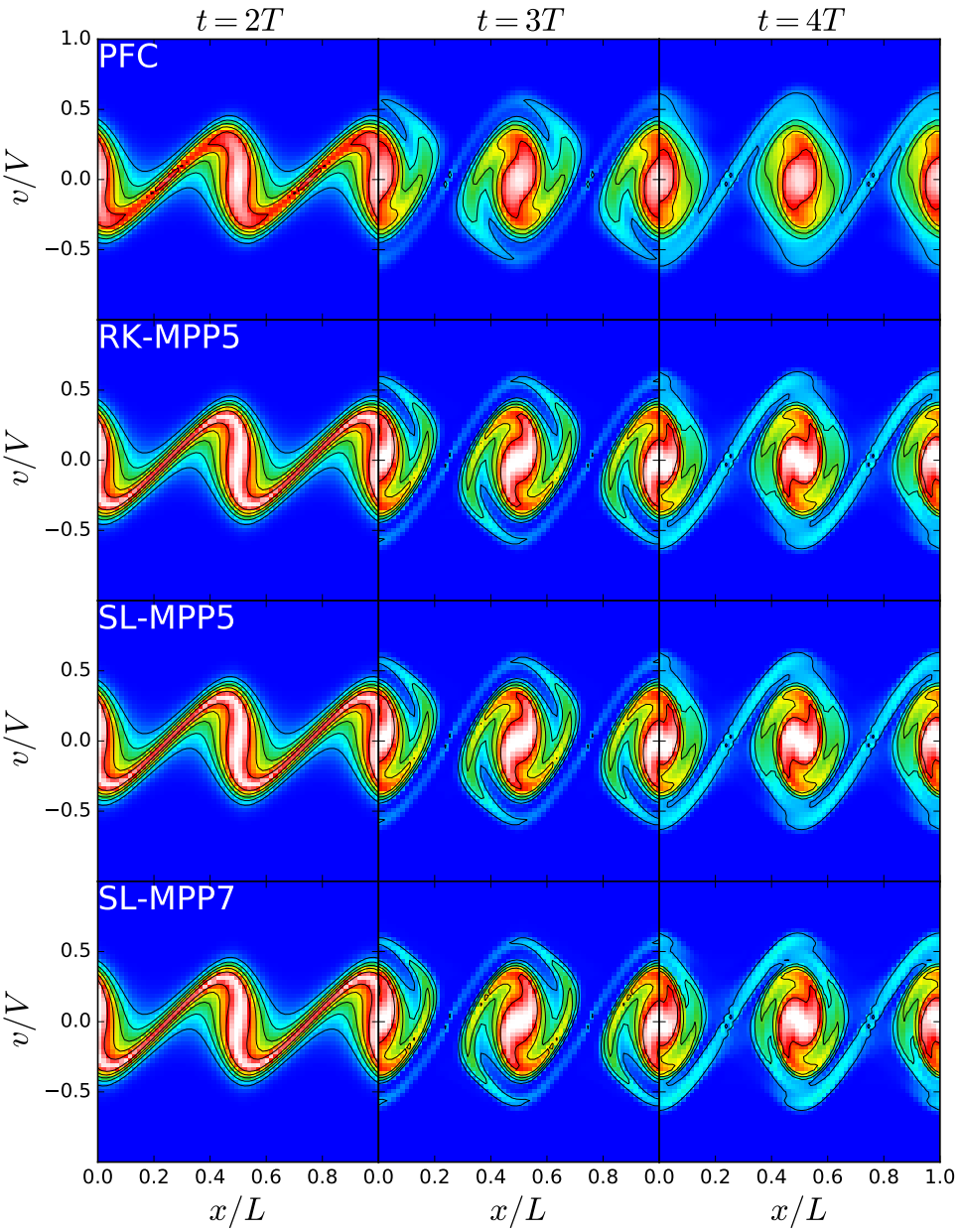

Figure 7. Test-2 (one-dimensional gravitational instability): Maps of the phase space density computed with PFC, RK–MPP5, SL–MPP5 and SL–MPP7 schemes from top to bottom at $t = 2T$, $3T$ and $4T$. We set $N_{\rm x} = N_{\rm v} = 64$.

In this test, we set the wavenumber k to $k = 4\pi/L$ and the velocity dispersion σ so as to be $k/k_{\rm J} = 0.5$, and the amplitude $A = 0.01$. The velocity space is defined over $-V \le v \le V$, where $V = L/T$ and T is the dynamical timescale defined by $T = (G\bar{\rho})^{-1/2}$. We adopt outflow boundary conditions in the velocity space. Figure 7 shows the maps of the phase space density computed with PFC, RK–MPP5, SL–MPP5 and SL–MPP7 at $t = 2T$, $3T$ and $4T$. The numbers of meshes in physical and velocity space are set to $N_{\rm x} = N_{\rm v} = 64$. The phase space density computed with PFC (with third-order reconstruction) is significantly smeared especially at later epochs compared to the results with other spatially higher-order schemes. The results with RK–MPP5 and SL–MPP5 schemes, both of which have the spatially fifth-order accuracy, appear almost identical to each other. SL–MPP7 clearly yields spiral-arm structure in the phase space located at the turn-around position.

Figure 8 compares the results computed by RK–MPP5, SL–MPP5 and SL–MPP7 with the PP limiter (upper panels) and by RK–MP5, SL–MP5 and SL–MP7 schemes without it (lower panels). The regions with negative phase space density depicted by white dots in the lower panels are not present in the results computed with the PP limiter.

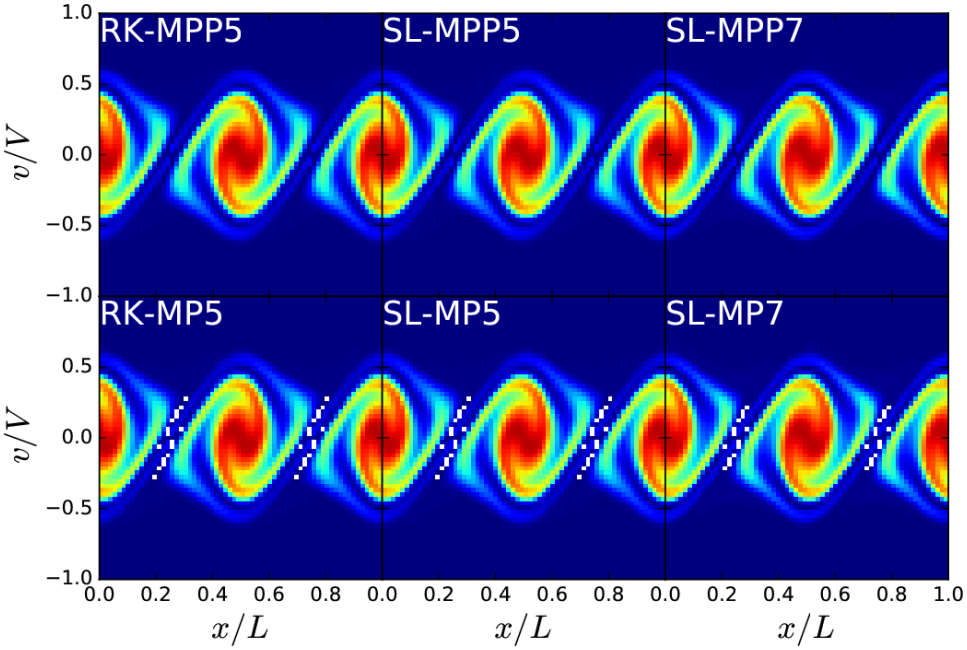

Figure 8. Test-2 (one-dimensional gravitational instability): Maps of the phase space density obtained by advection schemes with and without the positivity preserving limiter. White regions in the lower panels have negative phase space density. We set $N_{\rm x} = N_{\rm v} = 64$.

To measure the accuracy of the numerical solutions obtained with various schemes, we compute the following quantity

$$\epsilon(t) = \frac{\sum_{i=1}^{N_{\rm x}} \sum_{j=1}^{N_{\rm v}} |f(x_i, v_j, t) - f_{\rm ref}(x_i, v_j, t)|}{\sum_{i=1}^{N_{\rm x}} \sum_{j=1}^{N_{\rm v}} |f_{\rm ref}(x_i, v_j, t)|}, \tag{67}$$

where $f_{\rm ref}(x, v, t)$ is a reference solution to be compared with. Since we do not have any analytical solution for this test, we adopt the numerical solution obtained with SL–MPP7 with a very large number of grids, $N_{\rm x} = N_{\rm v} = 2048$, as the reference solution $f_{\rm ref}(x, v, t)$. Figure 9 shows the relative errors of the numerical solutions at $t = 4T$ with $N_{\rm x} = N_{\rm v} = 64$, 128, 256, 512 and 1024 for PFC, RK–MPP5, SL–MPP5, SL–MPP7 schemes. The accuracies of RK–MPP5, SL–MPP5 and SL–MPP7 schemes for a given number of mesh grids are much better than that of PFC with the same number of meshes, and are similar to. or even better than those of PFC scheme four times as many number of meshes.

3.3. *Test-3: Landau Damping in Electrostatic Plasma*

We perform simulations of Landau damping in an electrostatic plasma, in which the time evolution of the distribution function of electrons is described by the following Vlasov equation

$$\frac{\partial f}{\partial t} + v \cdot \frac{\partial f}{\partial x} - \frac{e}{m} \frac{\partial \phi_{\rm s}}{\partial x} \cdot \frac{\partial f}{\partial v} = 0, \tag{68}$$

where $\phi_{\rm s}$ is the electrostatic potential, and e and m is the charge and mass of an electron, respectively. The electrostatic potential satisfies the Poisson equation

$$\nabla^2 \phi_{\rm s} = 4\pi n e \left(1 - \int_{-\infty}^{\infty} f dv\right), \tag{69}$$

where n is the number density of ions. In this formulation, the distribution function is normalized such that its integration over the velocity space gives the fraction of electron number density relative to ions.

We consider a two-dimensional phase space with $-2\pi L \le x \le 2\pi L$ and $-6V \le v \le 6V$, where $V \equiv \omega_{\rm pe} L$ and $\omega_{\rm pe} = (4\pi e^2 n/m)^{1/2}$ is the electron plasma frequency and the periodic boundary condition is imposed on the physical

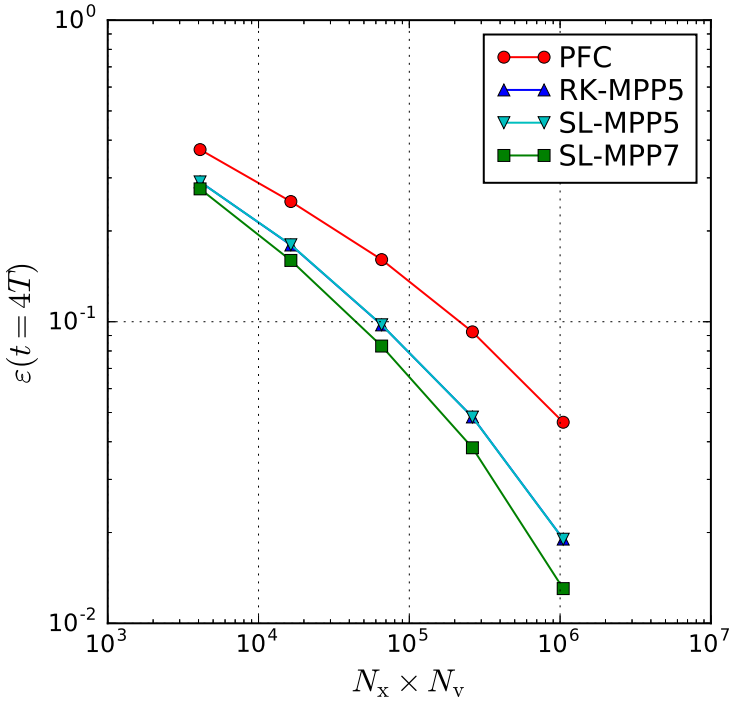

Figure 9. Test-2 (one-dimensional gravitational instability): Relative errors of numerical solutions relative to the reference solution as a function of number of mesh grids.

space. The initial condition is given by

$$f(x, v, t = 0) = \frac{1}{\sqrt{2\pi\sigma^2}} \exp\left(-\frac{v^2}{2\sigma^2}\right)(1 + A\cos kx), \tag{70}$$

where the wave number is set to $k = 1/(2L)$ and $\sigma = V$. With this initial condition, it is expected that the electric field damps exponentially as $\exp(-\gamma\omega_{\rm pe}t)$ with $\gamma = 0.153$.

First, we show results of linear Landau damping in which we set the amplitude of the initial perturbation to $A = 0.01$. We set $N_{\rm x} = N_{\rm v} = 64$. Figure 10 shows time evolution of the amplitude of the electric field with a mode of $k = 1/(2L)$ obtained with PFC and SL–MPP5. The results obtained with RK–MPP5 and SL–MPP7 are almost the same as that of SL–MPP5 and are not presented in this figure. Although the numerical solution with PFC ceases to damp at $t \gtrsim 40\omega_{\rm pe}^{-1}$, the one obtained with the SL–MPP5 scheme continues to damp to $t \lesssim 55\omega_{\rm pe}^{-1}$, just before the recurrence time $t_{\rm R} = 2\pi/(k\Delta v) = 67\omega_{\rm pe}^{-1}$; SL–MPP5 is less dissipative than PFC.

Next, we perform simulations of non-linear Landau damping with $A = 0.5$. This problem has been investigated in a number of previous studies (e.g., Klimas 1987; Manfredi 1997; Nakamura & Yabe 1999). In this problem, the initial perturbations damp (in space) quickly, but a highly stratified distribution in the phase space develops with time through rapid phase mixing (see Figure 11). The amplitude of the electric field initially decreases, but particle trapping by the electric field prevents complete dispersion. Figure 11 shows the phase space density of electrons at $t = 10\,\omega_{\rm pe}^{-1}$, $20\,\omega_{\rm pe}^{-1}$, $40\,\omega_{\rm pe}^{-1}$, and $50\,\omega_{\rm pe}^{-1}$ computed with PFC, RK–MPP5, SL–MPP5 and SL–MPP7. All the results are obtained with $N_{\rm x} = 64$ and $N_{\rm v} = 256$. Rapid phase-space mixing generates a number of peaks along the velocity axis. The PFC solution exhibits a smeared distribution at $t \gtrsim 40\,\omega_{\rm pe}^{-1}$, while those computed with other higher order schemes preserve features of phase mixing even at $t = 50\,\omega_{\rm pe}^{-1}$. This is also seen in Figure 12 in which we show the velocity distribution function

$$F(v, t) = \int f(x, v, t)dx \tag{71}$$

at $t = 50\,\omega_{\rm pe}^{-1}$. There are a number of peaks in the velocity distribution function, which represent electrons trapped by electrostatic waves around their phase velocities. The peaks in the distribution function are more prominent in the results with fifth- and seventh-order schemes than in PFC, again showing the less dissipative nature of our schemes.

3.4. *Test-4: Spherical Collapse of A Uniform Density Sphere*

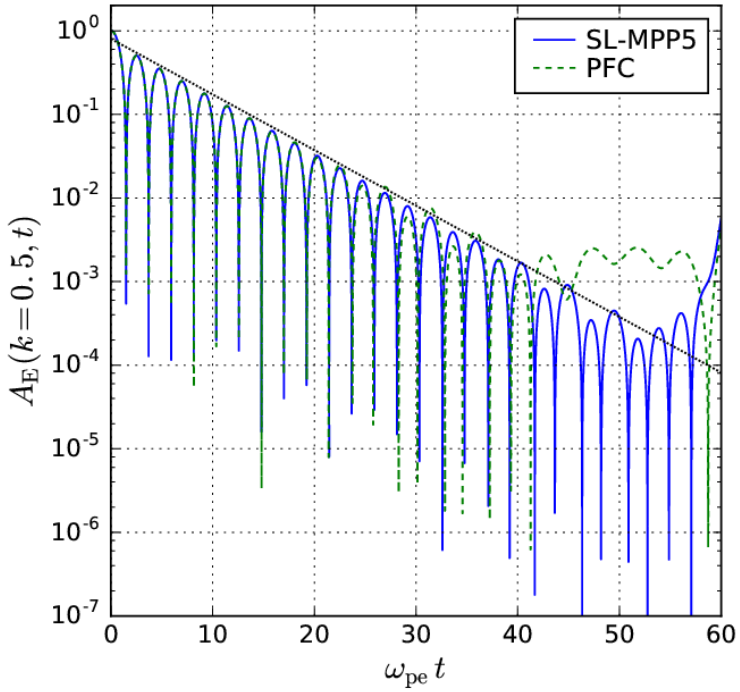

Figure 10. Test-3 (Landau damping in electrostatic plasma): Time evolution of the amplitude of the electric field normalized at $t = 0$. The dotted line indicates the theoretical prediction with a damping rate of $\gamma = 0.153$. We set $N_{\rm x} = N_{\rm v} = 64$.

Finally, we study gravitational collapse of a uniform density sphere. The mass and the initial radius of the sphere is M and $2R$, respectively, and the initial distribution function is given by

$$f(\boldsymbol{x}, \boldsymbol{v}, t = 0) = \frac{\rho_0}{(2\pi\sigma^2)^{3/2}} \exp\left(-\frac{|\boldsymbol{v}|^2}{2\sigma^2}\right), \tag{72}$$

where $\rho_0 = M/(4\pi(2R)^3/3)$ is the initial density of the sphere and $\sigma^2 = GM/(20R)$ is the initial velocity dispersion of the matter inside the sphere. We set the initial virial ratio to be 0.5. The extent of the simulation volume is $-3R \le x, y, z \le 3R$ in the physical space and $-3V \le v_x, v_y, v_z \le 3V$, where V is given by $V = R/T$ and $T = (R^3/GM)^{1/2}$ is the dynamical timescale of the system. In this test, we adopt the out-going boundary condition both in the physical and velocity spaces. We perform the runs with $N_{\rm x} = 64^3$ for the physical space and $N_{\rm v} = 32^3$ or $N_{\rm v} = 64^3$ mesh grids for the velocity space.

We plot the phase space density in the (x, v_x)-plane with $y = z = 0$ and $v_y = v_z = 0$ at $t = 3T$, $4T$, $6T$ and $8T$ in Figure 13. We set $N_{\rm x} = N_{\rm v} = 64^3$. Initially, the sphere starts to collapse toward the center, and reaches the maximum contraction around $t = 4T$. Then the system expands again, and a part of the matter passes through the center of the system to reaches the outer boundary defined at a distance of $3R$ from the center. The results computed with PFC shows smeared distribution compared with those obtained with RK–MPP5, SL–MPP5 and SL–MPP7. We note that RK–MPP5 and SL–MPP5 yield almost identical results, although the computational costs for the two are significantly different.

Figure 14 is the same plot as Figure 13 but shows the results with $N_{\rm v} = 32^3$. With the effectively low resolution, we can see the differences between the spatially fifth- and seventh-order schemes. It is interesting that the results obtained by SL–MPP7 scheme with $N_{\rm x} = 64^3$ and $N_{\rm v} = 32^3$ (bottom panels in Figure 14) are similar to or even better than those obtained with PFC with $N_{\rm x} = N_{\rm v} = 64^3$, despite the eight times smaller number of mesh grids (top panels in Figure 13).

For this test, we compare our schemes with another independent scheme. To this end, we utilize a high-resolution N-body simulation in the following manner. First, we perform an N-body simulation starting from the initial condition equivalent to equation (72). In this N-body simulation, the gravitational potential field is dumped and stored at all the time steps. Then, we compute the phase space density of a given phase space coordinate $(\boldsymbol{x}(t), \boldsymbol{v}(t))$ by tracing back the coordinate to its initial coordinate $(\boldsymbol{x}(0), \boldsymbol{v}(0))$ using the previously stored gravitational potentials. Since the phase space density is constant along each trajectory, we can, in principle, compute the phase space density from the initial phase space coordinate $(\boldsymbol{x}(0), \boldsymbol{v}(0))$ using equation (72). However, trajectories in conventional N-body simulations are

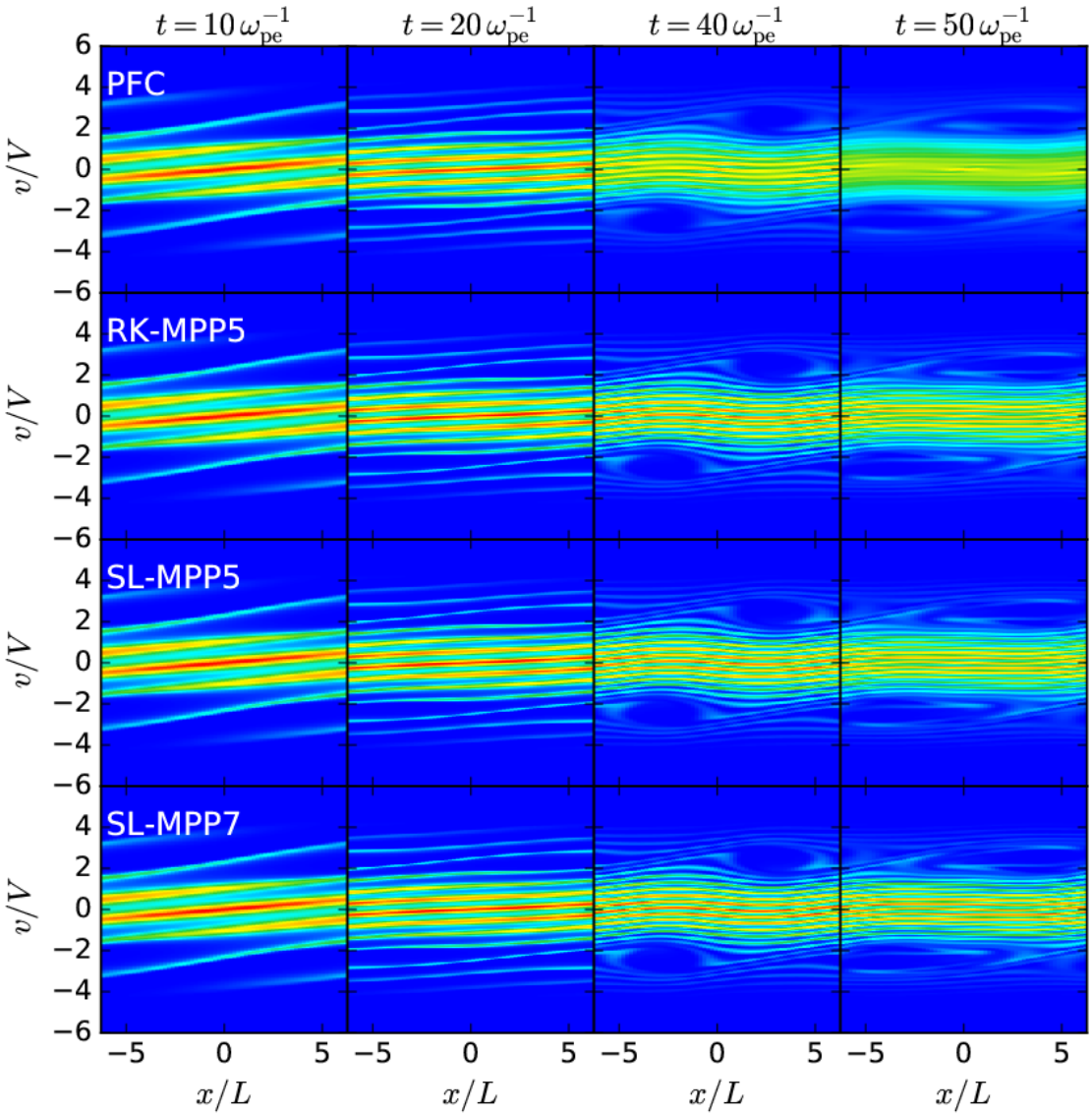

Figure 11. Test-3 (Landau damping in electrostatic plasma): Maps of the phase space density of electrons in non-linear Landau damping computed with PFC, RK–MPP5, SL–MPP5 and SL–MPP7 schemes (from top to bottom) at $t = 10\omega_{\rm pe}^{-1}$, $20\omega_{\rm pe}^{-1}$, $40\omega_{\rm pe}^{-1}$ and $50\omega_{\rm pe}^{-1}$ (from left to right). Numbers of mesh grids in physical and velocity spaces are set to $N_{\rm x} = 64$ and $N_{\rm v} = 256$, respectively.

subject to rather grainy gravitational potential than what it should be in the actual physical system due to their super-particle approximation. Thus, we adopt the self-consistent field (SCF) method (Hernquist & Ostriker 1992; Hozumi 1997), in which the gravitational potential is computed by expanding the density field into a set of basis functions, and particle trajectories are calculated for the *smooth* gravitational potential. The initial condition is constructed with 10^7 equal mass particles, and the particle orbits are computed using the basis set constructed by Clutton-Brock (1972), where the numbers of the expansion terms are 64 in radial direction, and 144 in angular directions, respectively. Figure 15 shows the phase space density computed with the above procedures. Comparing with Figures 13 and 14 manifests that our spatially higher-order schemes (RK–MPP5, SL–MPP5 and SL–MPP7 schemes) yield results much closer to those obtained with the combined N-body and SCF approach. It should be noted that, in practice, the SCF method is applicable only to self-gravitating systems with a certain spatial symmetry, such as in the present test, to which the lowest order functions of the basis set suffice to describe the overall structure of the system. Also, storing the gravitational potential (or its expansion) at all the time steps is very costly. Therefore, the above combined approach cannot be applied to a wide range of self-gravitating systems.

We further examine the mass and energy conservation for this spherical collapse test. We show the time evolution of the total mass, kinetic and gravitational potential energy of the results simulated with PFC and SL–MPP5 in

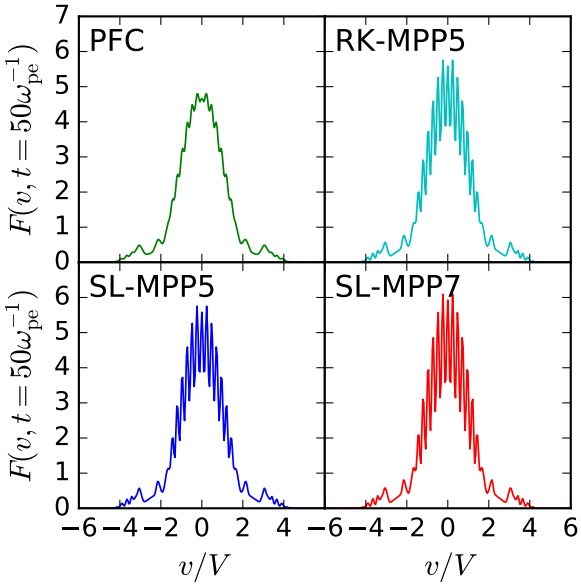

Figure 12. Test-3 (Landau damping in electrostatic plasma): Velocity distribution functions in non-linear Landau damping at $t = 50\omega_{\rm pe}^{-1}$ computed with PFC, RK–MPP5, SL–MPP5 and SL–MPP7 schemes. The results are computed using the phase space density shown in Figure 11.

Figure 16, where the results obtained with $N_{\rm v} = 64^3$ and $N_{\rm v} = 32^3$ are shown in the left and right panels, respectively. Note that the results simulated with RK–MPP5 and SL–MPP7 are almost the same as that of the SL–MPP5 and hence are not shown in this figure. For comparison, we also plot the results obtained with an N-body simulation, in which we adopts the Particle-Mesh (PM) method with the number of mesh grids in solving the Poisson equation equal to that of the Vlasov–Poisson simulation, i.e., 64 mesh grids in each dimension, in order to realize the same spatial resolution of the gravitational field and force. We employ 128^3 particles. The total mass in the Vlasov simulation starts to decrease around $t = 8T$ because a part of the matter reaches the boundary of the simulation volume at that time, as can be seen in Figure 15. In the runs with the PFC scheme, such decrease of the total mass begins earlier and the amount of the escaped mass is larger than those in the runs with the SL–MPP5 and other higher-order schemes due to larger numerical diffusion, irrespective of $N_{\rm v}$. The most prominent difference can be seen around the maximum contraction epoch $t \simeq 4T$, when the kinetic and gravitational potential energy have their maximum and minimum values, respectively. As can be seen in Figure 15, the large numerical diffusion of PFC, both in the physical and velocity spaces, smears the "S"-shaped phase space distribution at $t = 4T$. Also the extent in the physical space gets larger, yielding the small kinetic energy and the shallow gravitational potential found in Figure 16. The result of SL–MPP5 is close to the N-body simulation. The overall accuracy can be increased for PFC, by simply increasing the resolution. In the runs with $N_{\rm v} = 64^3$, both of the results with the PFC and SL–MPP5 schemes are in good agreement with the N-body simulation. This suggests that SL–MPP5 (as well as RK–MPP5 and SL–MPP7) with $N_{\rm v} = 32^3$ provides roughly the same level of accuracy as PFC with $N_{\rm v} = 64^3$ in terms of mechanical energy.

4. COMPUTATIONAL COST

In addition to the overall computational accuracy, we need to address the computational speed of our schemes. We measure the wall-clock time to advance each of equations (4) and (5) by a single time step using PFC, RK–MPP5, SL–MPP5 and SL–MPP7 for various combinations of $N_{\rm x}$ and $N_{\rm v}$ ranging from 32^3 to 128^3 on 64 nodes of HA-PACS system at Center for Computational Sciences, University of Tsukuba. The largest number of mesh grids adopted in this test is $(N_{\rm x}, N_{\rm v}) = (128^3, 64^3)$. Figure 17 shows the measured wall-clock time per mesh grid in six-dimensional Vlasov–Poisson simulations of the growth of gravitational instability from a nearly uniform density distribution identical to Test-4 in YYU13. We show the wall-clock time to advance the advection equations in the physical space (equation (4)) and those in the velocity space (equation (5)) in left and right panel, respectively. One can see that RK–MPP5 is the most computationally expensive among all the advection schemes described in this work. This is largely because it performs three-stage RK time integration (see equation (10)) and compute numerical fluxes three times per step while other schemes need only single-stage time integration. Since the physical space is divided into sub-domains and stored in independent memory spaces, solving advection equations (4) in the physical space requires inter-node communications

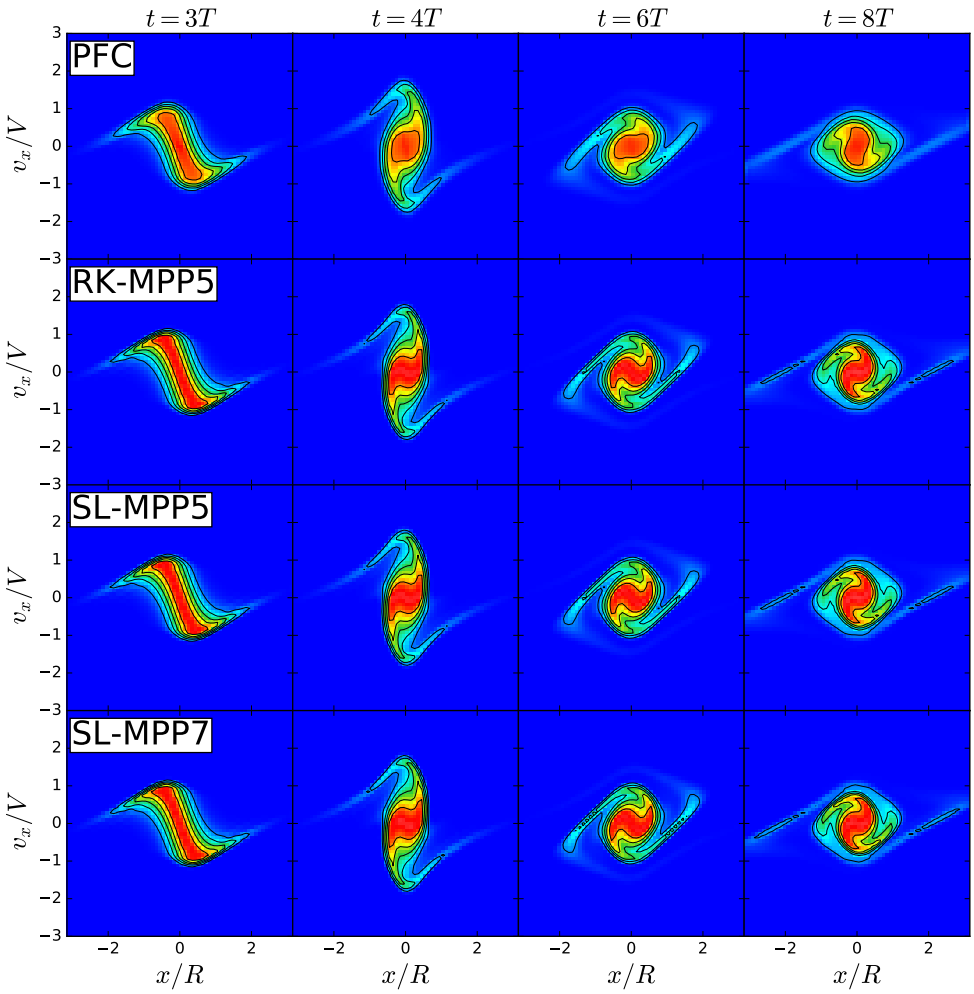

Figure 13. Test-4 (spherical collapse of a uniform density sphere): phase space density in the (x,v_x)-plane with $y = z = 0$ and $v_y = v_z = 0$ computed with PFC, RK–MPP5, SL–MPP5 and SL–MPP7 schemes at $t = 3T$, $4T$, $6T$ and $8T$. The number of mesh grids is 64^3 in the physical space and 64^3 in the velocity space.

to transfer phase-space densities to/from adjacent computational nodes, and thus takes a longer wall-clock time than solving equations (5) in the velocity space. The computational costs of SL–MPP5 and SL–MPP7 are significantly smaller than that of RK–MPP5, and are almost the same as PFC scheme.

5. SUMMARY AND CONCLUSION

In this work, we present a set of new spatially fifth- and seventh-order advection schemes developed for Vlasov simulations which preserve both of monotonicity and positivity of numerical solutions. The schemes are based on the spatially fifth-order monotonicity-preserving (MP) scheme combined with the three-stage TVD Runge-Kutta (TVD-RK) scheme proposed by Suresh & Huynh (1997), and are extended so that they also preserve positivity by using a flux-limiter. In addition, the semi-Lagrangean (SL) time integration is adopted instead of three-stage TVD-RK scheme, which improves the accuracy of time integration significantly without increasing the computational cost.

We perform an extensive set of numerical tests to verify the improvement of numerical solutions of Vlasov simulations using our newly developed schemes. The test suite includes one-dimensional linear advection problems, one-dimensional collisionless self-gravitating and electrostatic plasma systems in two-dimensional phase space, and a three-dimensional self-gravitating system in six-dimensional phase space. The results are compared with those obtained with the spatially third-order positive-flux-conservative (PFC) scheme adopted in our previous work (Yoshikawa et al. 2013), and summarized as follows.

In Test-1, we present calculations of one-dimensional linear advection problems and confirm that numerical solutions computed with the present schemes have better accuracy than the PFC scheme while the the seventh-order TVD-RK MP scheme exhibits undesirable features in the advection of a rectangular shaped function. The positivity preserving

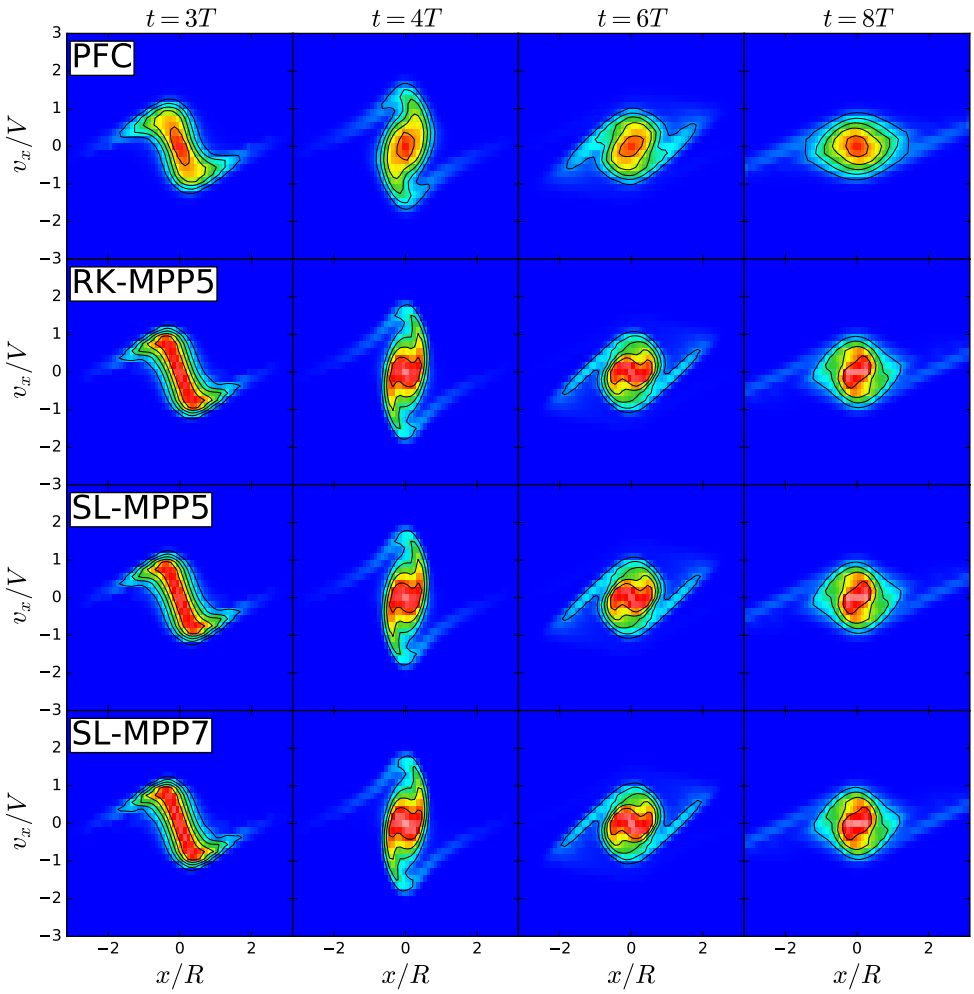

Figure 14. Test-4 (spherical collapse of a uniform density sphere): same as Figure 13 except that the number of mesh grids in the velocity space is 32^3.

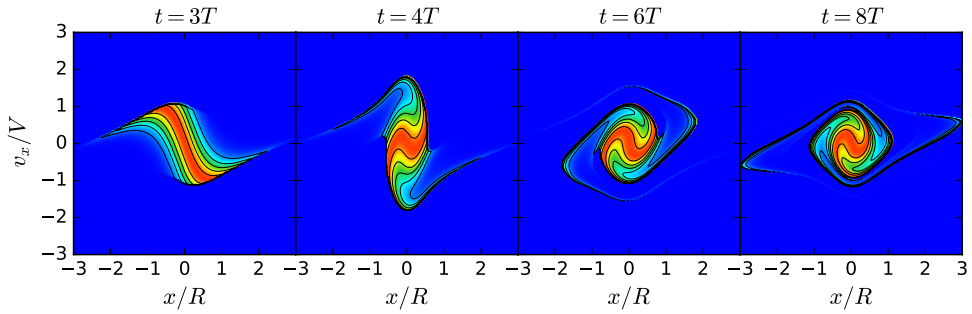

Figure 15. Test-4 (spherical collapse of a uniform density sphere): same as Figure 13 except that the self-consistent field method is used instead of the Vlasov–Poisson simulation.

limiter works well in every advection test in this work, although it introduce a slight degrade of numerical accuracy in terms of the error scaling in combination with TVD Runge-Kutta time integration scheme. It is found that the SL time integration provides us with better numerical accuracy than the TVD-RK scheme and that the combination of the positivity preserving limiter and the SL time integration does note introduce any expense of numerical accuracy unlike the TVD-RK time integration.

In Test-2 and Test-3, we perform Vlasov–Poisson simulations of a one-dimensional self-gravitating and electrostatic plasma systems in two-dimensional phase space, respectively. In the self-gravitating system, we found that the phase space density distribution simulated with the PFC scheme is significantly suffered from numerical diffusion compared

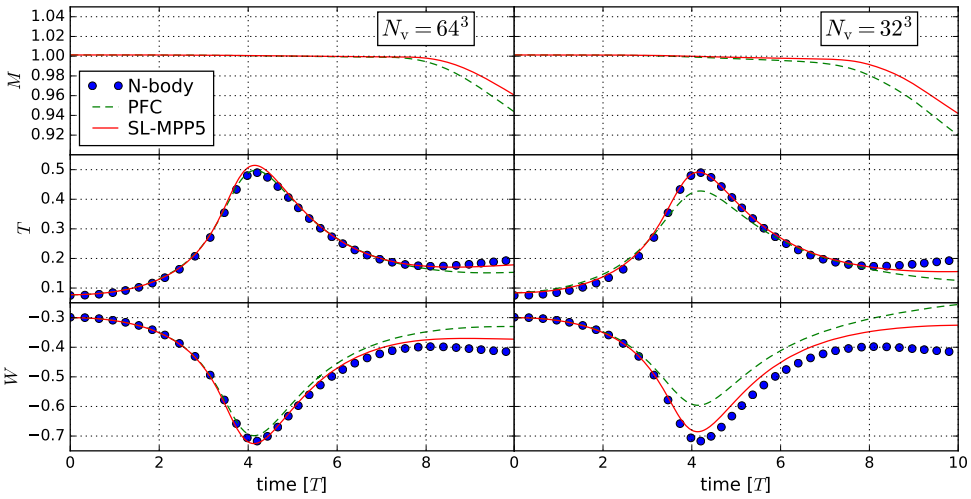

Figure 16. Test-4 (spherical collapse of a uniform density sphere): time evolution of the total mass (top), kinetic energy (middle) and potential energy (bottom) in the runs with $N_v = 64^3$ (left) and $N_v = 32^3$ (right) computed with the PFC and SL–MPP5 schemes. The kinetic and gravitational potential energy obtained with an N-body simulation are also shown for the comparison.

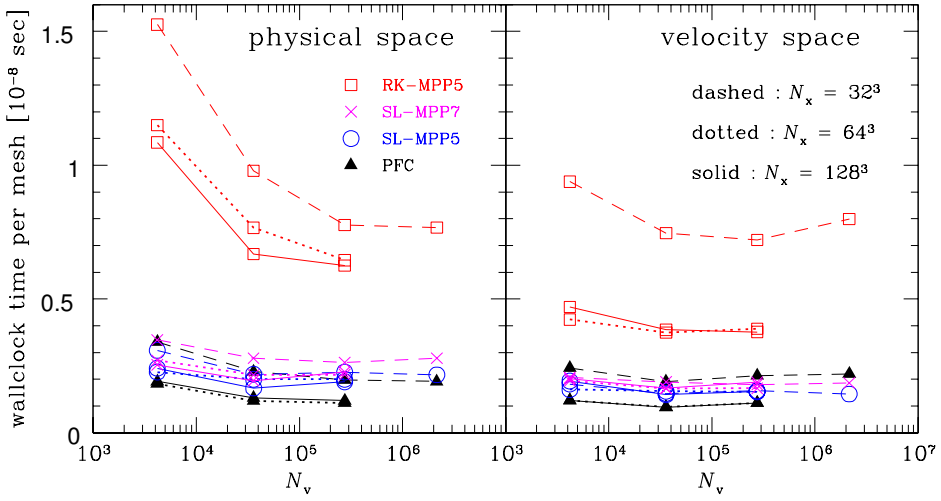

Figure 17. Wall-clock times per mesh grid for a single step of advection in the physical space (left panel) and the velocity space (right panel) computed with the PFC (filled triangles), RK–MPP5 (open squares), SL–MPP5 (open circles) and SL–MPP7 (crosses) schemes. Data connected with solid, dotted and dashed lines are measured in runs with $N_x = 32^3$, 64^3 and 128^3, respectively.

with the present schemes. In terms of the L^1 error of the distribution function, the fifth-order schemes yield almost identical results, and achieve almost the same level of numerical accuracy of the third-order scheme with four times refined mesh grids, while the the seventh-order scheme is proved to be the most accurate scheme among all the schemes presented in this work. In addition, the positivity preserving limiter also works well in the Vlasov simulations. In the simulations of electrostatic plasma, we perform the linear and non-linear Landau damping problems. In the former, we found that numerical solution computed with the third-order scheme ceases damping sufficiently before the recurrence time due to its large numerical diffusion. On the other hand, the numerical solutions with the present schemes continue to damp just before the recurrence time. As for the non-linear Landau damping, highly stratified distribution formed through rapid phase mixing is in the numerical solution obtained with the third-order scheme due to the numerical diffusion.

Finally in Test-4, we perform Vlasov–Poisson simulations of a fully three-dimensional self-gravitating system in a six-dimensional phase space, in which runs with two different sets of numerical resolution $(N_x, N_v) = (64^3, 64^3)$ and $(N_x, N_v) = (64^3, 32^3)$ are conducted. By comparing the distribution functions obtained with the Vlasov–Poisson simulation with the one computed by exploiting the results with the reference solution obtained by the self-consistent field (SCF) method, one can see that the present schemes yield better numerical solutions than the third-order scheme, and

the advantage of these schemes are confirmed also in Vlasov simulations in six-dimensional phase space. Comparison of the results between the runs with two different numerical resolutions tell us that present schemes yield numerical numerical solutions equivalent to that obtained by the third-order scheme with eight times refined mesh grids.

As for the computational costs of our new schemes, TVD-RK scheme is most expensive and requires 2–3 times longer wall-clock time to advance a single time step than other schemes. This is mainly because it adopts the three-stage TVD-RK time integration scheme and operates the Eulerian time integration three times per step. On the other hand, the SL schemes perform only a single Eulerian time integration per step, hence, their computational costs are significantly less expensive than TVD-RK scheme and are nearly the same as that of PFC scheme, indicating that SL schemes achieve the improvement of effective spatial resolution without significant expense of computational costs.

Among all the new schemes described in this paper, seventh-order SL scheme is the most favored one in terms of numerical accuracy and computational cost, although the spatially fifth-order SL scheme can be a viable option when the capacity of inter-node communication is not very sufficient. As a similar scheme to SL schemes, Qiu & Christlieb (2010) and Qiu & Shu (2011) develop conservative semi-Lagrangian WENO schemes to solve Vlasov equation which adopt Weighted Essentially Non-Oscillatory (WENO) reconstruction to compute the interface values instead of the MP reconstruction adopted in our schemes. The WENO reconstruction is, however, known to be more diffusive and more computationally expensive compared with the MP scheme (Suresh & Huynh 1997).

Since Vlasov simulations require huge amount of memory to store the distribution function in six-dimensional phase space volume, the size of Vlasov simulations is mainly limited by the amount of total available memory rather than the computational cost. Adoption of spatially higher order advection schemes in Vlasov simulations enables us to effectively improve the numerical resolution without increasing the number of mesh grids. In this sense, our new spatially high-order advection schemes are of crucial importance in numerically solving Vlasov equations. We implement our new advection schemes to Vlasov–Poisson simulations which can be applied to collisionless self-gravitating and electrostatic plasma systems, and confirmed that our schemes really improve the numerical accuracies of the Vlasov–Poisson simulations for a given number of mesh grids. Though we have applied our schemes only to Vlasov–Poisson simulations, we are going to apply our schemes to Vlasov–Maxwell simulations for magnetized plasma systems as a future work, in which difficulties in following gyro motion around magnetic field lines, or an advection by rigid rotation in velocity space have been reported by many authors (Minoshima et al. 2011, 2013, 2015).

We thank Professor Shunsuke Hozumi for providing distribution function data of Test-4 computed with his SCF code, and for his valuable comments on this work. This research is supported by MEXT as Priority Issue on Post-K computer (Elucidation of the Fundamental Laws and Evolution of the Universe) and JICFuS, and uses computational resources of the K computer provided by the RIKEN Advanced Institute for Computational Science through the HPCI System Research project (Project ID:hp120286). A part of numerical simulations are performed using HA-PACS and COMA systems at Center for Computational Sciences, University of Tsukuba, and Cray XC30 at Center for Computational Astrophysics, National Astronomical Observatory of Japan.

REFERENCES

Abel, T., Hahn, O., & Kaehler, R. 2012, MNRAS, 427, 61
Birdsall, C. K., & Langdon, A. B. 1991, Plasma Physics via Computer Simulation
Clutton-Brock, M. 1972, Ap&SS, 16, 101
Filbet, F., Sonnendrücker, E., & Bertrand, P. 2001, Journal of Computational Physics, 172, 166
Fujimoto, K. 2014, Geophys. Res. Lett., 41, 2721
Fujiwara, T. 1981, PASJ, 33, 531
Hahn, O., Abel, T., & Kaehler, R. 2013, MNRAS, 434, 1171
Hernquist, L., & Ostriker, J. P. 1992, ApJ, 386, 375
Hockney, R. W., & Eastwood, J. W. 1981, Computer Simulation Using Particles
Hozumi, S. 1997, ApJ, 487, 617
Hu, X. Y., Adams, N. A., & Shu, C.-W. 2013, Journal of Computational Physics, 242, 169
Janin, G. 1971, A&A, 11, 188
Kates-Harbeck, J., Totorica, S., Zrake, J., & Abel, T. 2016, Journal of Computational Physics, 304, 231
Klimas, A. J. 1987, Journal of Computational Physics, 68, 202
Manfredi, G. 1997, Physical Review Letters, 79, 2815
Matsumoto, Y., Amano, T., Kato, T. N., & Hoshino, M. 2015, Science, 347, 974
Minoshima, T., Matsumoto, Y., & Amano, T. 2011, Journal of Computational Physics, 230, 6800
—. 2013, Journal of Computational Physics, 236, 81
—. 2015, Computer Physics Communications, 187, 137
Mitchell, N. L., Vorobyov, E. I., & Hensler, G. 2013, MNRAS, 428, 2674
Nakamura, T., & Yabe, T. 1999, Computer Physics Communications, 120, 122
Nishida, M. T., Yoshizawa, M., Watanabe, Y., Inagaki, S., & Kato, S. 1981, PASJ, 33, 567
Qiu, J.-M., & Christlieb, A. 2010, Journal of Computational Physics, 229, 1130
Qiu, J.-M., & Shu, C.-W. 2011, Journal of Computational Physics, 230, 863
Shandarin, S., Habib, S., & Heitmann, K. 2012, PhRvD, 85, 083005
Suresh, A., & Huynh, H. 1997, Journal of Computational Physics, 136, 83
Vorobyov, E. I., & Theis, C. 2006, MNRAS, 373, 197

APPENDIX

A. MONOTONICITY PRESERVING CONSTRAINT

The MP scheme devised by Suresh & Huynh (1997) computes the interface value $f^{\rm MP}_{i+1/2}$ at a mesh boundary between the i- and $(i+1)$-th mesh grids with five stencil values, three in the upwind side and two in the downwind side in the following procedures:

1. Evaluate the interpolated interface value $f^{\rm int}_{i+1/2}$ at a mesh interface using equation. In the case of MP5 or MP7 schemes, for example, we adopt equations (9) or (24) in the fifth or seventh order accuracy, respectively.

2. Evaluate $f^* = f_i + {\rm minmod}(f_{i+1} - f_i, \alpha(f_i - f_{i-1}))$, where a parameter α controls the upper bound of the interface value and should hold the condition $\alpha \geq 2$. Throughout in this work, we set $\alpha = 4$, unless otherwise stated.

3. If the condition $(f^{\rm int}_{i+1/2} - f_i)(f^{\rm int}_{i+1/2} - f^*) < 0$ holds, the resultant interface value is given by $f^{\rm MP}_{i+1/2} = f^{\rm int}_{i+1/2}$. If not, we should proceed to the next step.

4. Compute $d^{\rm M4}_{i+1/2} \equiv {\rm minmod}(4d_i - d_{i+1}, 4d_{i+1} - d_i, d_i, d_{i+1})$ and $d^{\rm M4}_{i-1/2}$, where $d_i = f_{i-1} + f_{i+1} - 2f_i$.

5. Compute $f^{\rm UL} \equiv f_i + \alpha(f_i - f_{i-1})$, $f^{\rm AV} \equiv (f_i + f_{i+1})/2$, $f^{\rm MD} \equiv f^{\rm AV} - d^{\rm M4}_{i+1/2}/2$ and $f^{\rm LC} \equiv f_i + (f_i - f_{i-1})/2 + 4d^{\rm M4}_{i-1/2}/3$

6. Compute $f^{\rm min} \equiv \max(\min(f_i, f_{i+1}, f^{\rm MD}), \min(f_i, f^{\rm UL}, f^{\rm LC}))$ and $f^{\rm max} \equiv \min(\max(f_i, f_{i+1}, f^{\rm MD}), \max(f_i, f^{\rm UL}, f^{\rm LC}))$.

7. Finally, the interface value is given by $f^{\rm MP}_{i+1/2} = {\rm median}(f^{\rm int}_{i+1/2}, f^{\rm min}, f^{\rm max})$.

It should be noted that the time step constraint to keep the monotonicity of numerical solutions depends on the parameter α and the CFL parameter should satisfy the condition (Suresh & Huynh 1997)

$$\nu \leq 1/(1+\alpha) = 1/5, \tag{A1}$$

if we set the parameter α to $\alpha = 4$ as recommended in Suresh & Huynh (1997), although $\nu = 0.4$ works well in practice. (see Appendix B for further argument on a viable range of the CFL parameter.)

B. CFL CONDITION

As noted in Appendix A, the choice of α and ν is rather heuristic in the MP scheme. Therefore, we also optimize the combination of α and ν in our new schemes RK–MPP5, SL–MPP5 and SL–MPP7 with the PP limiter in a heuristic manner. We perform the Test-1c (linear advection of $\sin^4(4\pi x)$) using RK–MPP5, SL–MPP5 and SL–MPP7 schemes with various combinations of α and ν. Number of mesh grids is set to 128. Figure B1 shows maps of relative L^1-errors of Test-1c obtained with the three schemes for $0 < \alpha < 5$ and $0 < \nu < 1$. Comparison of RK–MPP5 and SL–MPP5 schemes shows that SL–MPP5 scheme allows us to adopt a larger CFL parameter ν than RK–MPP5 scheme to achieve a certain accuracy. Furthermore, errors obtained with SL–MPP5 scheme are almost unchanged irrespective to the adopted CFL parameter as long as $2 < \alpha$ and $\nu < 0.4$, probably in virtue of its semi-Lagrangian nature. SL–MPP7 scheme exhibits more accurate results than SL–MPP5 scheme for $2 < \alpha$ and $\nu < 0.4$, and the parameter space which yields the most accurate results is located in the vicinity of the relation $\nu = 1/(1+\alpha)$.

C. THE HIGH-ORDER POISSON SOLVER

We derive the green function of the discretized Poisson equation in spatially second-, fourth- and sixth-order accuracy. Here, just for the simplicity, we only consider the one-dimensional Poisson equation. The extension to the multi-dimensional one is quite straightforward. Given the discrete density field ρ_j with $0 \leq j \leq N_{\rm m} - 1$, where $N_{\rm m}$ is the number of mesh grids, approximating the Poisson equation with the second-order discretization leads to

$$\frac{\phi_{j+1} - 2\phi_j + \phi_{j-1}}{\Delta x^2} = 4\pi G \rho_j. \tag{C2}$$

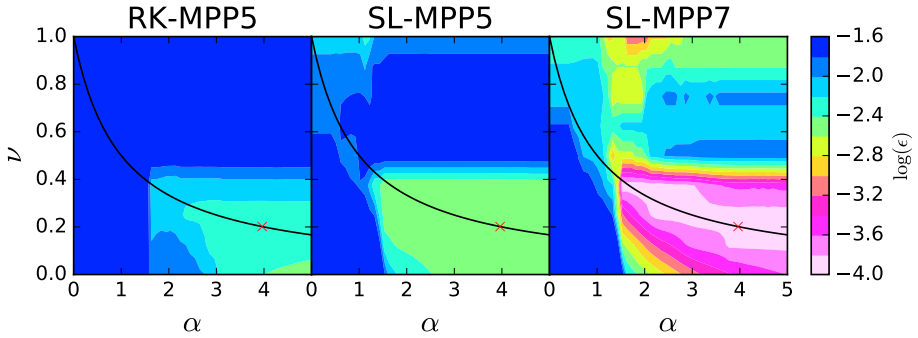

Figure B1. Maps of relative L^1-errors of Test-1c obtained with RK–MPP5 (*left*), SL–MPP5 (*middle*) and SL–MPP7 (*right*) schemes for ranges of $0 < \alpha < 5$ and $0 < \nu < 1$. Solid curves and red crosses indicate the relation $\nu = 1/(1+\alpha)$ and $(\alpha, \nu) = (4, 0.2)$, respectively.

Discrete Fourier transformation (DFT) of equation (C2) yields

$$\hat{\phi}_k[\exp(ik\Delta x) - 2 + \exp(-ik\Delta x)] = 4\pi G\Delta x^2 \hat{\rho}_k \tag{C3}$$

and $\hat{\phi}_k$ can be expressed as

$$\hat{\phi}_k = -\frac{\pi G\Delta x^2}{\sin^2\left(\dfrac{k\Delta x}{2}\right)}\hat{\rho}_k, \tag{C4}$$

where the 'hat' denotes the DFT of the physical quantities expressed as

$$\hat{q}_k = \sum_{j=0}^{N_\mathrm{m}-1} q_j \exp(-ikj\Delta x), \tag{C5}$$

and $k = 2\pi n/(N_\mathrm{m}\Delta x)$ is the discrete wavenumber, and the periodic boundary condition $\phi_j = \phi_{N_\mathrm{m}+j}$ is assumed. The discrete Poisson equations in the fourth- and sixth-order accuracy are given by

$$\frac{-\phi_{j+2} + 16\phi_{j+1} - 30\phi_j + 16\phi_{j-1} - \phi_{j-2}}{12\Delta x^2} = 4\pi G\rho_j \tag{C6}$$

and

$$\frac{2\phi_{j+3} - 27\phi_{j+2} + 270\phi_{j+1} - 490\phi_j + 270\phi_{j-1} - 27\phi_{j-2} + 2\phi_{j-3}}{180\Delta x^2} = 4\pi G\rho_j, \tag{C7}$$

respectively. Therefore, the corresponding Fourier transformed potentials can be derived as

$$\hat{\phi}_k = \frac{12\pi G\Delta x^2}{\sin^2(k\Delta x) - 16\sin^2(k\Delta x/2)}\hat{\rho}_k \tag{C8}$$

and

$$\hat{\phi}_k = -\frac{180\pi G\Delta x^2}{2\sin^2\left(\dfrac{3k\Delta x}{2}\right) - 27\sin^2(k\Delta x) + 270\sin^2\left(\dfrac{k\Delta x}{2}\right)}\hat{\rho}_k, \tag{C9}$$

respectively.

Gravitational force is numerically obtained with the finite difference approximation (FDA) of gradient of the gravitational potential. Use of the higher-order Poisson solvers motivates us to adopt higher-order FDAs for the gravitational force. The gradient of the gravitational potential at $x = x_i$ is approximated as

$$\nabla\phi|_{x=x_i} = \frac{\phi_{i+1} - \phi_{i-1}}{2\Delta x} + O(\Delta x^2), \tag{C10}$$

$$\nabla\phi|_{x=x_i} = \frac{\phi_{i+2} - 8\phi_{i+1} + 8\phi_{i-1} - \phi_{i-2}}{12\Delta x} + O(\Delta x^4), \tag{C11}$$

and

$$\nabla\phi|_{x=x_i} = \frac{\phi_{i+3} - 9\phi_{i+2} + 45\phi_{i+1} - 45\phi_{i-1} + 9\phi_{i-2} - \phi_{i-3}}{60\Delta x} + O(\Delta x^6) \tag{C12}$$

with the two-, four- and six-point FDA, respectively.

To check the numerical accuracy of the gravitational potential and force obtained with the numerical schemes described above, we solve the one-dimensional Poisson equation with the periodic boundary condition under the density field given by

$$\rho(x) = \bar{\rho}\left[1 + A\sin(kx)\right], \tag{C13}$$

in the domain $0 \leq x < L$ where the wavenumber k is set to $k = 32\pi/L$, and we have 16 waves in the domain. The gravitational potential and force can be analytically solved as

$$\phi(x) = -\frac{4\pi G\bar{\rho}A}{k^2}\sin(kx) \tag{C14}$$

and

$$f(x) = -\frac{\partial\phi(x)}{\partial x} = \frac{4\pi G\bar{\rho}A}{k}\cos(kx), \tag{C15}$$

respectively. Figure C2 shows the relative errors of gravitational potentials and forces defined by

$$\epsilon_{\rm pot} = \frac{1}{N_{\rm m}}\sum_{j=0}^{N_{\rm m}-1}|\phi_j - \phi(x_j)| \tag{C16}$$

and

$$\epsilon_{\rm f} = \frac{1}{N_{\rm m}}\sum_{j=0}^{N_{\rm m}-1}|f_j - f(x_j)|, \tag{C17}$$

respectively. Note that the gravitational forces are computed with a FDA scheme with the same order of accuracy as the Poisson solver, i.e., the gravitational forces with the second-order accuracy are computed with the gravitational potentials calculated with the second-order Poisson solver through the second-order FDA scheme. It can be seen that both of the gravitational potentials and forces have the expected order of the accuracy.

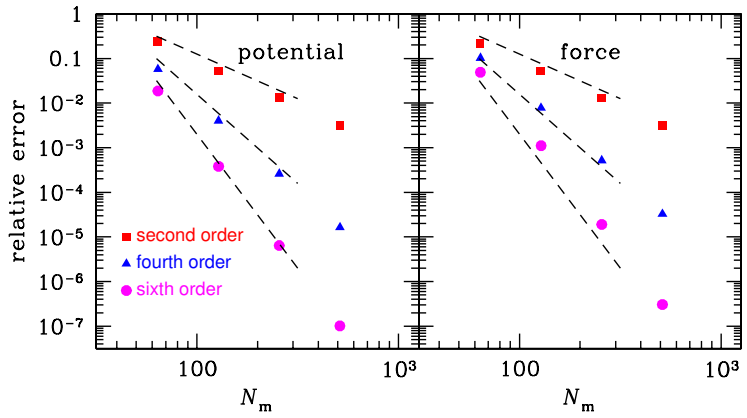

Figure C2. Relative errors of gravitational potentials (left panel) and forces (right panel) computed with spatially second-, fourth- and sixth-order scheme for $N_{\rm m} = 64, 128, 256$ and 512. Dashed lines show the scalings of the second, fourth, and sixth accuracies from top to bottom.